Energy Response of the SNO Detector in the Presence of the Neutral Current Detector Array

A.W.P. Poon, S.R. Elliott, and R.G.H. Robertson

Nuclear Physics Laboratory, University of Washington, Seattle, WA 98195, USA

SNO-STR-97-010

Abstract

In this report, we compare the energy response of the SNO detector in the pure D_2O and the Neutral Current Detector (NCD) array installed running scenarios. We demonstrate a "gain correction" technique to correct for the positional and directional dependence of the SNO detector response. This technique can reliably reconstruct energy spectra in both running scenarios. The vertex and directional fitting performance of the time fitter is investigated for the two running scenarios. A systematic effect of enhanced Čerenkov output in the acrylic vessel for gamma rays generated close to the vessel is also discussed.

Contents

1 Introduction

One of the fundamental advantages offered by the installation of the Neutral Current Detector (NCD) array is its ability to separate and to distinguish neutral current and charged current signals on an event-by-event basis. In fact, all the backgrounds and signals can be determined simultaneously. Unlike other neutral current detection schemes involving chemical additives to the D_2O these unique features of the NCD array eliminate some of the complication of subtracting a background signal taken at different times under different detector operating conditions.

These advantages do not come without a cost. In terms of Čerenkov signal extraction in the presence of the NCD array, photons will be scattered and absorbed by the surface of the counters, thereby reducing the number of photons detected by the photomultiplier tube array. This reduction of the number of detected photons reduces the photon statistics for event fitters in the offline analysis and impacts the detector resolution. Also one would expect the response of the photomultiplier tube array to have a stronger dependence on the position of the event vertex and the direction of the outgoing particle when the NCD array is in place.

In this report, we shall investigate the response of the photomultiplier array in the presence of the NCD array. We accomplish this task by comparing the detector response in both the pure D_2O and the NCD installed running scenarios. We shall demonstrate that the introduction of the NCD array *does not* compromise the photomultiplier array's efficiency in detecting electron events originated in the active D_2O volume. We shall also show that the installation of the NCD array *does not* have a significant effect on the efficiency of vertex and direction fitting in the offline analysis. Furthermore, we shall introduce a "gain correction" algorithm to account for the positional and directional dependence of the detector response in the presence of the NCD array.

2 SNOMAN Monte Carlo Configuration

2.1 NCD Configuration

The NCD array consists of 96 strings of ^{3}He proportional counters deployed on a square lattice of 1 metre spacing. The body of the counters is made up of chemical vapour deposited (CVD) nickel, which has an ultra-low radioactivity. Each of these strings is a concatenation of one or more individual ^{3}He counters.

In this Monte Carlo study, we use version 2.09 of the program SNOMAN [1]. In this version, each string is modelled as nickel cylinders oriented vertically with a 1-metre lattice constant. Given that we are mostly concerned with signals external to the Ncdarray in this study, the geometry of the mechanical components internal to the counter body of each string is ignored.

Optical characteristics of the Ncdarray' surface finish is critical to this study. Waltham [2] had measured the total reflectance of the CVD nickel-water interface in the visible regime using a spectrophotometer. This measurement was made on nickel samples before any chemical treatment. The total reflectance of the CVD nickel surface in water varies smoothly from about 1.5% at 300 nm to about 6% at 600 nm. One of us (AWPP) incorporated this data into SNOMAN 2.09 by

using a polynomial fit of the data to generate the diffuse reflectance.

The total reflectance of the CVD nickel is noticeably higher after the chemical etching procedure. The purpose of this cleaning procedure is to remove surface contamination incurred during the CVD nickel manufacturing process. At the time of writing this report, the total reflectance of the etched nickel samples has not been measured. However, the overall effect of using the reflectance of unetched nickel would merely be a gain shift in the detector's energy response. Therefore, the conclusions of this report are not very much affected by this systematic uncertainty.

2.2 Other Software Configurations

SNOMAN is a sophisticated program capable of simulating the SNO detector in many different configurations and complexities. In order to strike a balance between the computing speed and the reliability of the results, we chose to use the *default* Monte Carlo configuration in SNOMAN 2.09 with a couple of minor changes.

In order to reduce the number of Čerekov photons to be tracked during program execution, the default configuration of SNOMAN renormalised the quantum efficiency of the photomultiplier tubes to unity, and the number of Čerenkov photons generated is reduced by a compensating factor CERFAC. The corresponding factor for the photomultiplier structure is CERFAC_II. To avoid the subtleties in interpreting the statistical significance of our results and the possible deviation from the true photomultiplier tube hit pattern, we chose to run with both CERFAC and CERFAC_II set to unity, that is, the quantum efficiency of the photomultiplier tubes is reset to its physical value.

We also use the full three dimensional models for the photomultipliers and the light concentrator petals, instead of the default grey disk model which has the average angular and wavelength response folded in.

In this version of SNOMAN, all the photomultipliers and associated electronics are treated to have the same operational characteristics. That is, the calibration constants for charge to photoelectrons are the same for all photomultiplier channels. In reality, these constants would be different for each channel.

3 SNO Detector Response

When the NCD array is in place, the main concern is whether or not the SNO detector can still take accurate data on the charged current signal. Lay has done some work in understanding the energy response of the SNO detector when the NCD array is in place [3]. In his study, he investigated the N_{hits} distribution for monoenergetic electrons and gamma rays as a function of energy. In this section, we shall extend Lay's work. In particular, we shall look at both the N_{hits} and the N_{pe} spectra in order to determine if there is any non-linear effect introduced by the NCD array. It is desirable to look at the energy dependence of both the N_{hits} and the N_{pe} distributions. One would expect multiple hits on a photomultiplier tube to be an important effect at high energy. However, one should not discount the fact that this multiple hit effect should also have a strong positional

3

dependence. For instance, an event originated near the photomultiplier array would be more likely to have more multiple hits if the electron travels towards the array.

To accomplish this task, we analyse monoenergetic electron and gamma-ray events generated by SNOMAN configured as described in sections 2.1 and 2.2. These isotropic events are evenly distributed in the D_2O volume. In this analysis, we look at the raw N_{hits} and N_{pe} recorded within the event time window. This allows us to isolate the effects of the NCD array on the fitter performance from those of the photomultiplier array response. In Section 4, we shall investigate the effect of the NCD array has on the time fitter performance.

3.1 Energy Response to Electrons and γ Rays — A Zeroth Order Approximation

As a first step, we look at the N_{hits} and N_{pe} distributions for monoenergetic, isotropic electrons and gamma rays generated evenly throughout the D_2O volume. The N_{pe} information is taken from the calibrated high gain, long time integrated channel output from SNOMAN. The N_{hits} and N_{pe} distributions at each energy are fitted to a Gaussian distribution to extract the means μ and the widths σ. In Table 1 and Table 2, we summarise the results for both pure D_2O and NCD installed configurations. The 1σ statistical uncertainties on the fitted means and the widths are <0.15% and 1% respectively.

We want to emphasise that the numbers listed in Table 1 and Table 2 are only "zeroth order approximations." As we shall see in Section 3.2, the photomultiplier tube array response depends on both the position of the event and the direction of the outgoing track. Hence, the results in Table 1 represent a gross average of the detector response which is an inadequate measure of the detector performance since the positional and directional dependencies are not taken into account. As we shall demonstrate later, these dependencies can be corrected for. It should also be noted that the results have a ~2% systematic uncertainty because of the presence of the belly plates and sanded joints in the real detector, which are not modelled in this study.

The results are displayed graphically in Figures 1 and 2. In these figures, we define the detector resolution as the quotient between the full-width-at-half-max and the mean:

$$\text{Resolution} = \frac{\Delta N_k}{N_k} = 2.354 \frac{\sigma_k}{\mu_k} \qquad k = hits, pe. \tag{1}$$

We want to point out several observations from this "zeroth approximation" analysis.

1. In the solar neutrino energy regime, N_{hits} varies roughly linearly with energy. A quadratic fit would provide a better fit. Lay [3] pointed out this same observation.

2. On the other hand, N_{pe} response is almost linear in the same energy regime. This strongly suggests that photomultiplier tubes are receiving multiple hits. In Figure 3 a plot of the average number of photoelectrons for every photomultiplier tube hit is shown. It is clear that this ratio increases substantially as the energy increases. However, one would find the shape of this line somewhat counter-intuitive. One would expect this ratio to remain relatively constant at low energy, and would increase gradually as energy increases. We reckon that

4

E_e	Pure D_2O				D_2O + NCD			
(MeV)	$\mu_{N_{hits}}$	$\sigma_{N_{hits}}$	$\mu_{N_{pe}}$	$\sigma_{N_{pe}}$	$\mu_{N_{hits}}$	$\sigma_{N_{hits}}$	$\mu_{N_{pe}}$	$\sigma_{N_{pe}}$
2	19.3	4.0	25.2	6.0	17.7	3.1	22.7	5.9
3	30.0	6.3	39.8	9.7	25.8	6.1	34.2	8.8
4	41.1	7.7	54.9	12.0	35.3	7.6	47.1	11.6
5	52.2	8.8	70.2	13.6	44.6	9.1	59.9	13.8
6	63.3	9.9	85.6	15.5	54.0	10.2	72.8	15.7
7	74.0	10.9	100.8	17.2	62.9	11.6	85.6	17.9
8	84.6	12.0	115.7	18.9	72.0	13.0	98.2	20.1
9	94.8	12.5	130.4	20.2	80.9	13.7	111.4	21.8
10	105.4	13.4	145.8	21.8	89.6	14.8	124.2	24.0
11	115.7	14.0	161.1	23.2	98.0	15.7	136.8	25.6
12	125.3	14.8	174.7	24.6	106.8	16.5	149.5	27.9
13	135.7	15.4	190.4	25.6	115.1	17.1	161.7	29.5
14	145.5	15.9	205.2	27.0	122.9	18.1	173.8	31.9
15	155.1	16.7	219.6	28.7	131.1	18.6	186.5	32.8
16	164.8	17.2	234.2	29.8	139.3	18.9	198.8	34.2
17	174.3	17.5	249.1	30.7	147.3	20.3	211.7	36.8
18	183.8	18.3	263.6	32.8	155.5	20.6	224.6	38.5
19	192.8	18.7	278.4	33.5	162.5	21.4	235.7	40.7
20	202.1	19.0	292.9	34.3	170.8	21.4	248.5	41.8
25	247.2	21.6	366.4	40.1	209.0	24.0	311.4	50.5

(Table title: Monoenergetic Electrons)

Table 1: Mean μ and width σ of N_{hits} and N_{pe} as a function of energy for monoenergetic electrons. Results for both pure D_2O and NCD installed scenarios are shown. These numbers are valid for isotropic electrons generated evenly throughout the D_2O volume. Because of the directional and the positional dependence of the detector response, these numbers should only be treated as a "zeroth order approximation." These numbers also have a $\sim 2\%$ systematic uncertainty because of the presence of the belly plates and sanded joints in the real detector, which are not modelled in this study.

Monoenergetic Gamma rays							
E_γ	Pure D_2O				D_2O + NCD			
(MeV)	$\mu_{N_{hits}}$	$\sigma_{N_{hits}}$	$\mu_{N_{pe}}$	$\sigma_{N_{pe}}$	$\mu_{N_{hits}}$	$\sigma_{N_{hits}}$	$\mu_{N_{pe}}$	$\sigma_{N_{pe}}$
2	15.5	2.5	19.9	4.6	14.5	2.0	19.1	4.3
3	22.1	5.5	29.1	7.9	20.3	4.1	25.8	7.0
4	30.8	8.0	40.7	12.0	26.9	7.7	35.7	11.0
5	41.3	9.6	55.4	14.0	35.4	9.2	47.5	13.3
6	52.0	10.9	70.4	16.1	44.4	10.2	59.7	15.4
7	62.2	11.7	84.5	17.5	53.4	11.6	72.1	17.1
8	72.7	12.9	99.3	19.7	62.8	12.5	85.2	19.2
9	83.4	13.6	114.3	21.0	71.3	13.4	97.1	20.5
10	94.1	14.2	129.3	22.3	80.4	14.9	110.3	22.9
11	104.2	14.8	144.0	23.5	89.2	16.1	122.9	25.2
12	114.2	15.6	158.4	25.2	98.0	17.0	135.6	26.5
13	124.5	16.5	172.9	26.5	106.8	18.1	148.2	28.8
14	134.9	16.8	188.6	27.8	115.2	18.8	160.9	30.0
15	144.9	17.4	203.5	28.9	123.8	19.8	173.3	31.9
16	154.8	17.9	218.0	29.8	132.8	20.6	187.5	34.5
17	164.6	18.1	232.8	31.0	140.4	21.4	198.8	36.5
18	174.4	18.7	247.8	32.5	149.1	22.1	211.8	37.6
19	184.5	19.2	262.9	33.0	157.3	22.6	224.0	39.2
20	193.8	19.4	276.8	34.1	165.4	23.6	236.5	41.1
25	240.5	21.9	351.9	40.1	205.0	26.4	299.8	50.5

Table 2: Mean μ and width σ of N_{hits} and N_{pe} as a function of energy for monoenergetic gamma rays. Results for both pure D_2O and NCD installed scenarios are shown. These numbers are valid for isotropic gamma rays generated evenly throughout the D_2O volume. Because of the directional and the positional dependence of the detector response, these numbers should only be treated as a "zeroth order approximation." These numbers also have a ~2% systematic uncertainty because of the presence of the belly plates and sanded joints in the real detector, which are not modelled in this study. The fits in both N_{hits} and N_{pe} cases are worse than the corresponding ones in the monoenergetic electron set in Table 1. This is because of the different responses from the gamma ray conversion in the acrylic vessel for gamma rays generated near to the vessel.
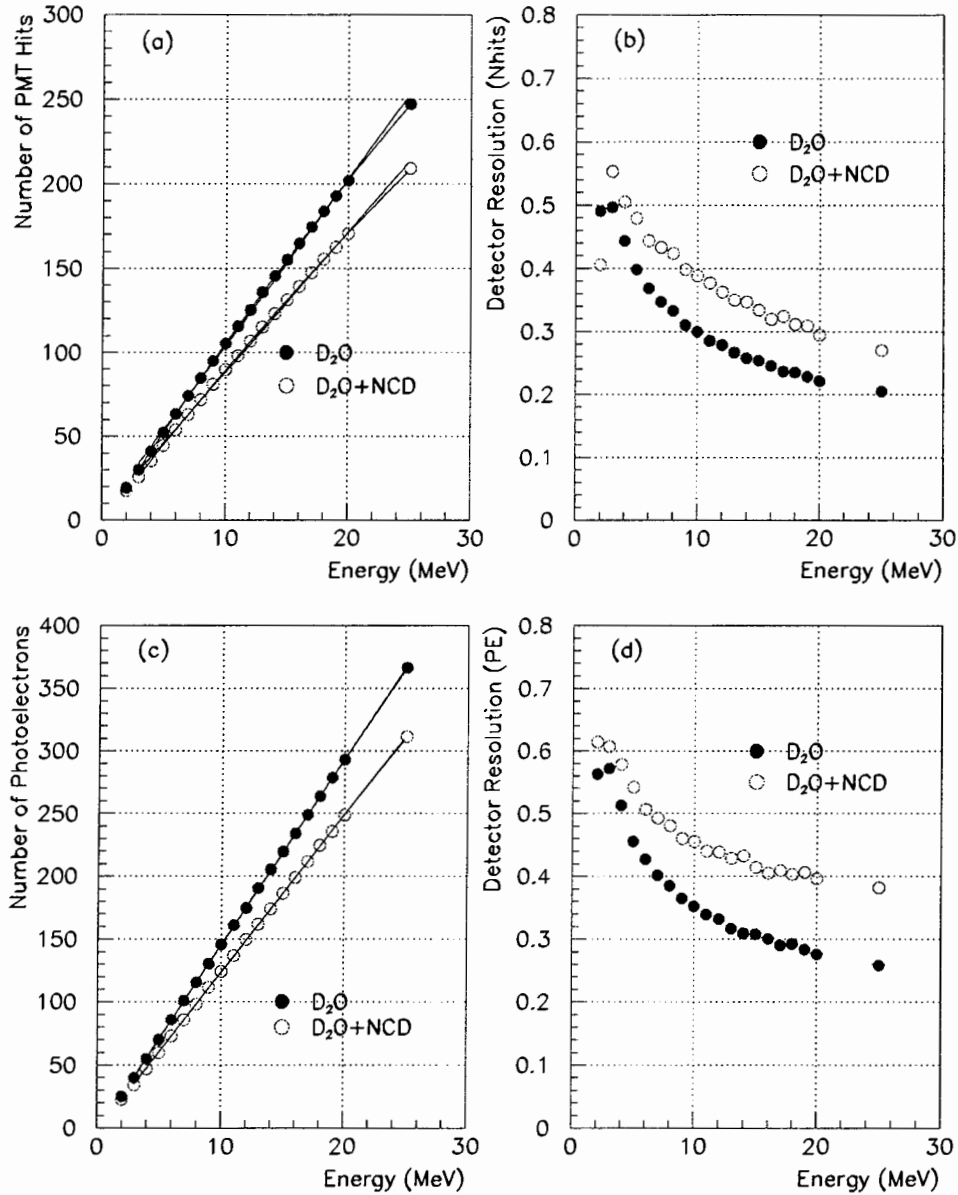
Monoenergetic Electrons

Figure 1: N_{hits} and N_{pe} energy calibration curve for monoenergetic electrons. The N_{hits} and N_{pe} distributions for each electron energy are fitted to a Gaussian distribution. (a) energy dependence on N_{hits}; (b) detector resolution dependence on electron energy calculated based on N_{hits} distributions; (c) N_{pe} dependence on electron energy; (d) detector resolution dependence on electron energy calculated based on N_{pe} distributions. The degradation of the detector resolution calculated based on N_{pe} is a consequence of the convolution of the charge resolution of the photomultiplier tubes to the N_{hits} spectrum. The lines are linear and quadratic fits to the energy calibration curve, with the quadratic curve giving a slightly better fit.
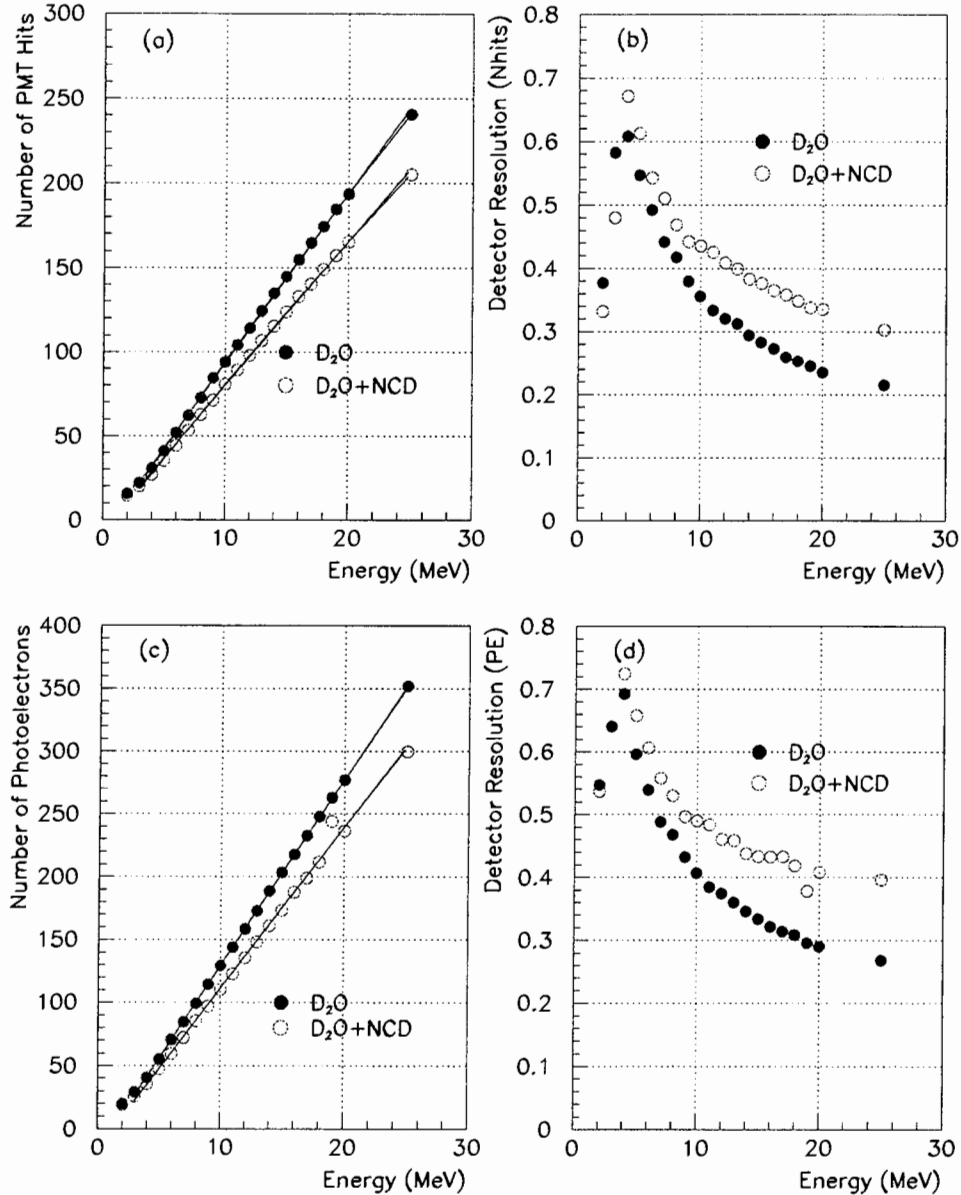
Monoenergetic Gamma-Rays

Figure 2: N_{hits} and N_{pe} energy calibration curves for monoenergetic gamma rays. The N_{hits} and N_{pe} distributions for each gamma-ray energy are fitted to a Gaussian distribution. (a) energy dependence of N_{hits} ; (b) detector resolution dependence on gamma-ray energy calculated based on N_{hits} distributions; (c) N_{pe} dependence on gamma-ray energy; (d) detector resolution dependence on gamma-ray energy calculated based on N_{pe} distributions. The degradation of the detector resolution calculated based on N_{pe} is a consequence of the convolution of the charge resolution of the photomultiplier tubes to the N_{hits} spectrum. The lines are linear and quadratic fits to the energy calibration curve, with the quadratic curve giving a slightly better fit.

8

this could be attributed to the fact that the calibrated charge from the electronics code, instead of the actual number of photoelectrons generated was used in this calculation. In actual SNO running, this calibrated charge would be the output of the electronics chain. We are investigating different techniques to "quantise" this calibrated charge to reflect the discrete number of photoelectrons that actually hit the photomultiplier tube array.

3. The detector resolution calculated using N_{pe} appears to be worse than that in the N_{hits} case in this "zeroth order approximation." This result is somewhat surprising as the resolution should improve as more information is fed to the analysis. This could be attributed to the fact that the calibrated charge, which has a rather broad distribution because of the poor charge resolution of the photomultiplier tubes, was used.

4. The detector resolution is degraded by $\sim$6 to $\sim$10% when the NCD array is present. However, as we shall demonstrate later, this "zeroth order approximation" analysis is inadequate in estimating the detector response because of its strong positional and directional dependencies.

5. The amount of light loss due to the presence of the NCD array is $\sim$15%. The energy dependence of light loss is displayed in Figure 4. We shall demonstrate later that this light loss has a strong positional and directional dependence which can be corrected for.

6. Both N_{hits} and N_{pe} signals are smaller for gamma rays comparing to electrons. The resolution for gamma rays is also worse. This is attributed to multiple Compton scattering.

7. Both N_{hits} and N_{pe} spectral fits at high energies are worse in the gamma-ray cases because of the long tail at large N_{hits} or N_{pe}. As we shall demonstrate later (see page 20), this tail arises from the gamma-ray conversion in the acrylic vessel.

However, these conclusions were reached based on a rather simple analysis. As we have pointed out earlier, these results should only be treated as "zeroth order approximations."

3.2 Energy Response to Electrons — Positional and Directional Dependence

One would expect the photomultiplier tube array response to have stronger positional and directional dependencies when the NCD array is in place. This response function should also depend on the direction of the Čerenkov cone as light absorption will be bigger for photons travelling a longer distance inside the D_2O volume. In Figure 5, we display how N_{hits} depends on the vertex position and the track direction for 10 MeV isotropic electrons generated evenly throughout the D_2O volume. The track direction is parameterised as $\cos(\delta)$ where δ is the opening angle between the position vector of the generated vertex and the generated direction of the outgoing track (Figure 6). That is, events with $\cos(\delta) \geq 0$ would be "outward" going, whilst those with $\cos(\delta) < 0$ would be "inward" going.

In Figure 5, it is evident that the "outward" going events, in which photons travel less distance than the "inward" going events, register more photomultiplier tube hits. In the case of the pure D_2O scenario, this can be explained by light attenuation of the D_2O and the acrylic vessel. The difference between the pure D_2O case and the NCD installed case is primarily light absorption by the NCD array. The directional dependence is noticeably stronger in the presence of the NCD array as evident in the increased slope of the scatter plot when comparing to the pure D_2O case.
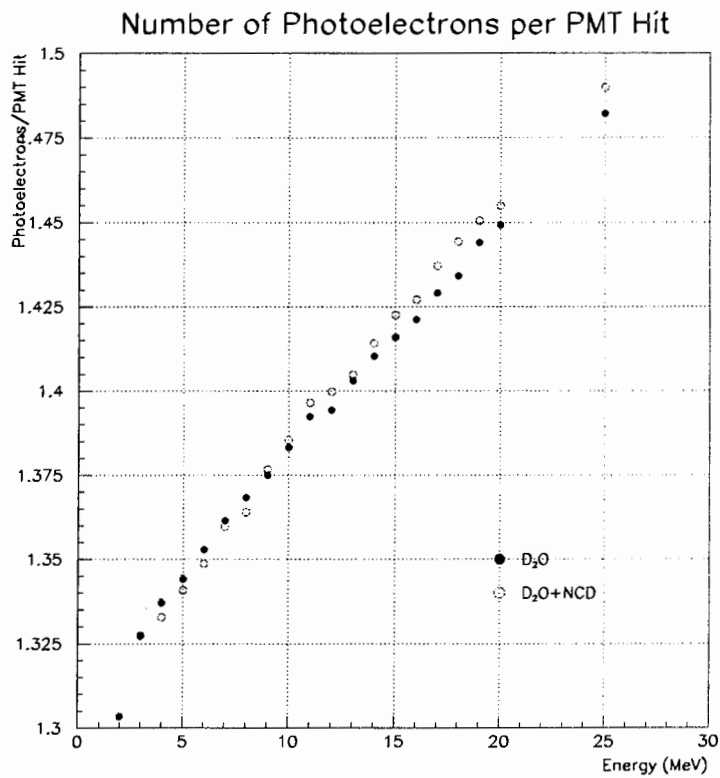
9

Figure 3: Number of photoelectrons (N_{pe}) per photomultiplier tube hit (N_{hits}) as a function of electron energy. The dependence for pure D_2O and for NCD installed scenarios are shown. This diagram clearly shows that photomultiplier tubes are registering more multiple hits as the event energy increases.
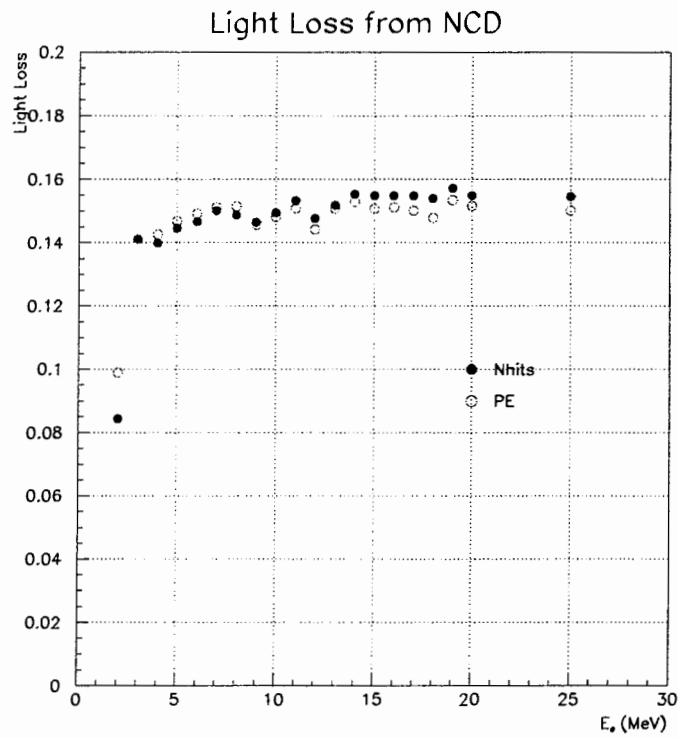
Figure 4: Fractional light loss as a function of electron energy in the NCD installed scenario. This light loss is shown as N_{hits} and N_{pe} reduction in the presence of the NCD array. The drop in light loss at 2 MeV is an artifact in fitting a Gaussian to the N_{hits} and N_{pe} spectra when a significant part of the spectra is below the hardware threshold of 10 hits.
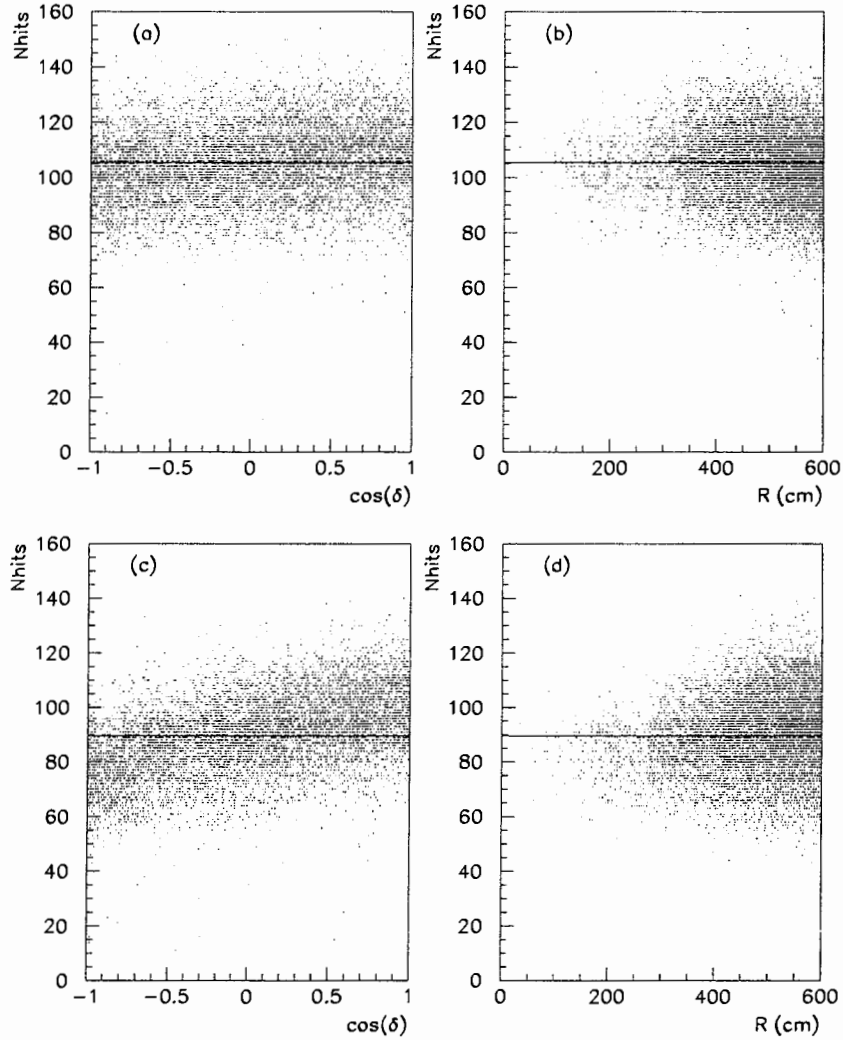
Figure 5: Scatter plot showing positional and directional dependence of N_{hits} distribution for 10000 10 MeV electron events generated isotropically and evenly throughout the D_2O volume. (a) N_{hits} dependence on the opening angle between the positional vector of the vertex and the direction of the electron track in pure D_2O scenario; (b) N_{hits} dependence on the radial distance of the vertex in pure D_2O scenario; (c) N_{hits} dependence on the opening angle between the positional vector of the vertex and the direction of the electron track in NCD installed scenario; (d) N_{hits} dependence on the radial distance of the vertex in NCD installed scenario. The horizontal lines drawn are the mean N_{hits} calculated based on the "zeroth order approximation" approach in the last section.
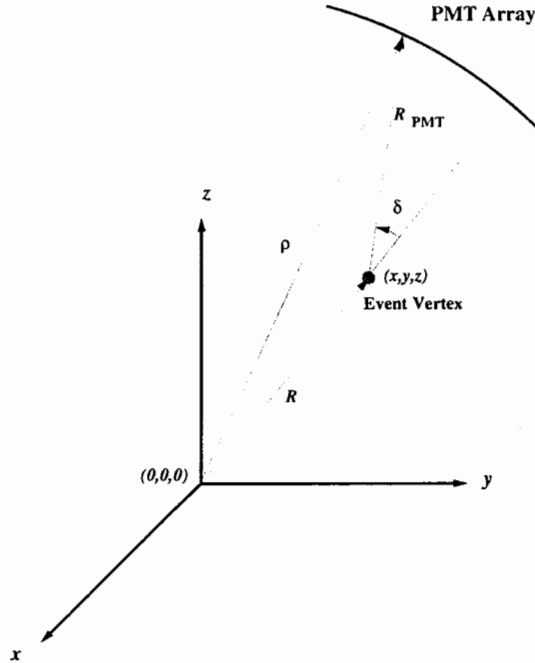
Figure 6: Definition of the parameter R_{PMT}. This parameter is the distance between the event vertex and the projected point at the photomultiplier array along the electron direction.

The positional dependence of N_{hits} is also stronger in the presence of the NCD array as the N_{hits}-R scatter plots show a less symmetric profile in the NCD installed case. Also shown as horizontal lines in Figure 5 are the mean N_{hits} for the two different detector operating conditions. The asymmetry of points about this line clearly indicates that the "zeroth order" fitting procedure in the previous section is inadequate for describing the energy response of the SNO detector in the NCD installed case.

As an attempt to account for both the directional and positional dependence, we construct a parameter R_{PMT} defined as

$$R_{PMT} = -R\cos\delta + \sqrt{(R\cos\delta)^2 + \rho^2 - R^2} \tag{2}$$

where R is the radial distance of the vertex, δ is opening angle between the generated electron direction and the radial vector of the generated vertex, and ρ is the radial distance of the photomultiplier array (890 cm). R_{PMT} is the distance between the event vertex and the projected point at the photomultiplier array along the electron direction. This parameter can be viewed as an estimation to the average distance the Čerenkov photons would travel. These definitions are shown in Figure 6.

The effect of light absorption by the NCD array can be analysed by comparing the difference in N_{hits} or N_{pe} dependence on R_{PMT} in the pure D_2O case and the NCD installed scenario. In Figure 7, the N_{hits} dependence on R_{PMT} for the same 10 MeV electron data set is shown for both of these scenarios. It is clear that as the Čerenkov photons travel more distance, the reduction in N_{hits} is more significant in the NCD installed scenario.
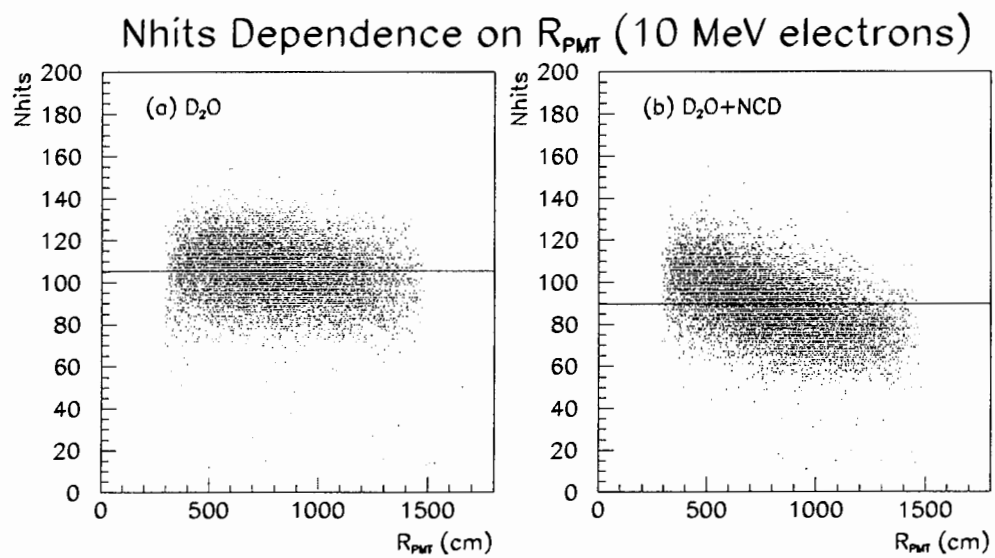
13

Figure 7: Scatter plot showing N_{hits} dependence on R_{PMT} . (a) pure D_2O ; (b) NCD installed. The horizontal lines shown here are the means calculated using the "zeroth order approximation" approach in the previous section.

E_e (MeV)	$\mu_{N_{hits}}$	$\sigma_{N_{hits}}$	$\mu_{N_{pe}}$	$\sigma_{N_{pe}}$
3	28.5	5.9	37.1	9.1
5	49.8	8.4	66.0	12.6
10	100.9	12.6	135.9	19.0
15	150.7	15.5	206.4	24.2

Table 3: Spectral information on the standard candle sets. The standard candles are monoenergetic electrons generated isotropically from the centre of the SNO detector. The resulting N_{hits} and N_{pe} spectra are fitted to Gaussian distributions to extract the means and the widths.

To compare the difference in R_{PMT} dependence between the pure D_2O and the NCD installed scenarios, R_{PMT} is divided into 50-cm bins. The resulting N_{hits} spectrum in each of these bins is fitted to a Gaussian distribution. In Figures 8, the fitted means $\mu(R_{PMT})$ and resolutions for the same 10 MeV electron data set used in Figure 5 are plotted in the pure D_2O and NCD installed scenarios.

In Figure 8, $\mu(R_{PMT})$ shows a maximum at $R_{PMT} \sim 500$ cm. In fact, the "peak" gets more and more pronounced as the electron energy increases. Although this "peak" does not seem to exist in the NCD installed case, it does appear at higher energies. The degradation of signal at higher R_{PMT} can be understood as increased light attenuation in the D_2O with longer propagation path. The drop in $\mu(R_{PMT})$ at small R_{PMT} is a manifestation of photomultiplier tubes receiving multiple hits. To demonstrate this last point, similar plots of N_{pe} for the same 10 MeV electron data set is shown in Figure 9. Notice that the "peak" has disappeared in these latter plots.

The positional and directional dependence of the detector resolution is vividly shown in Figure 8. The difference between $\mu(R_{PMT})$ of pure D_2O and of NCD installed cases demonstrates that light loss through absorption by the NCD surface is more significant than light attenuation in the heavy water. As a result, the detector resolution gets worse rather rapidly at higher R_{PMT} when the NCD is in place. Later, we shall demonstrate a "gain correction" technique to more properly handle the "inward" and "outward" going events.

The R_{PMT} dependence of $\mu(R_{PMT})$ can be seen as a gain variation in the detector. One can therefore correct for the gain by comparing the signals in both operating scenarios to a "standard candle." We define the gain correction factor at each energy as

$$G_\alpha^i(R_{PMT}) = \frac{\mu_\alpha^o}{\mu^i(R_{PMT})}, \qquad i = D_2O, NCD; \alpha = N_{pe}, N_{hits} \qquad (3)$$

where μ_α^o is the extracted mean of N_{hits} for the "candle," $\mu_{D_2O}(R_{PMT})$ and $\mu_{NCD}(R_{PMT})$ are the extracted mean of N_{hits} or N_{pe} at a particular R_{PMT} for the pure D_2O and the NCD installed scenarios. In this analysis, we have used 3 MeV, 5 MeV, 10 MeV and 15 MeV monoenergetic electrons generated isotropically at the centre of the SNO detector as standard candles. The N_{hits} and N_{pe} spectra of the candle sets are fitted to a Gaussian distribution to extract μ_α^o for that candle. In Table 3, we list the spectral information on the standard candle sets.

In principle, $G_\alpha^i(R_{PMT})$ should be an energy independent geometrical factor. However, as we have pointed out earlier, the effect of multiple hits causes a drop in N_{hits} at small R_{PMT}. This effect is,
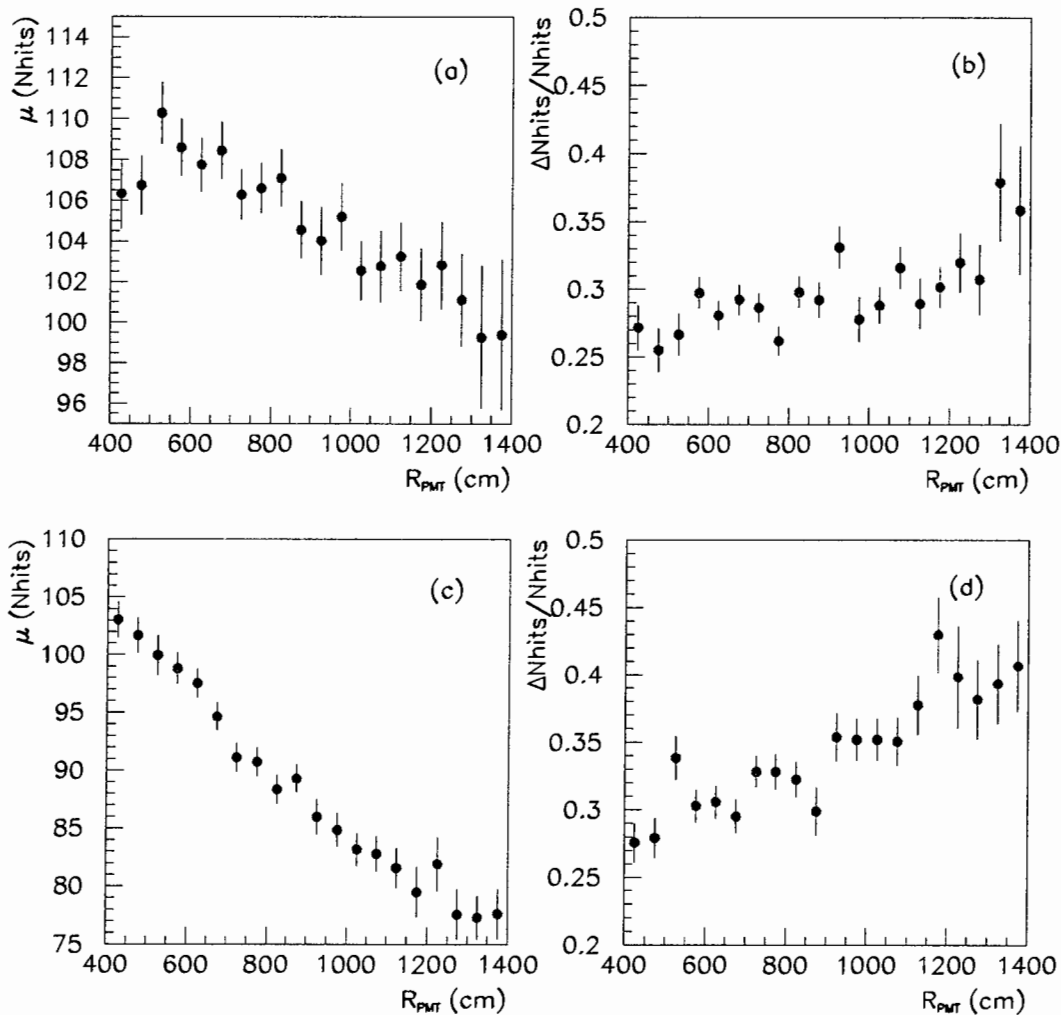
15

Figure 8: Plots showing the mean and the resolution as functions of R_{PMT} for 10 MeV electrons in pure D_2O and in the NCD array installed detector. (a),(b): N_{hits} centroid and resolution as functions of R_{PMT} in the pure D_2O scenario; (c), (d): N_{hits} centroid and resolution as functions of R_{PMT} in the NCD installed scenario.
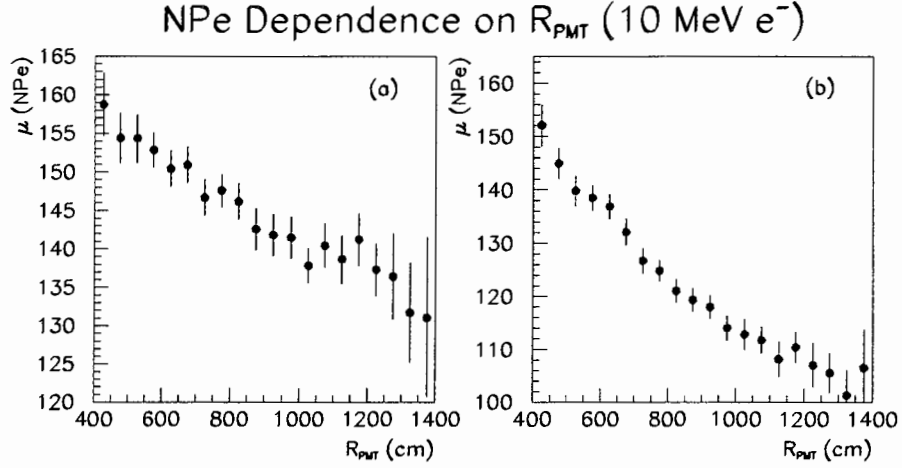
NPe Dependence on R_{PMT} (10 MeV e$^-$)

Figure 9: $\mu(R_{PMT})$ calculated based on N_{pe} . The "peak" structure at $R_{PMT} \sim 500$cm is now gone.

however, non-linear and might be energy dependent. In Figure 10, $G^i_\alpha(R_{PMT})$ is extracted using N_{hits} information and is plotted against electron energy. It is clear that at low R_{PMT} the shape of this gain correction function is very much dependent on the energy of the calibration "candle." The difference in the shape of $G^i_\alpha(R_{PMT})$ amongst the candle sets is attributed to multiple hits at small R_{PMT}.

To try eliminating the effect of multiple hits, we repeat the analysis by using the means in the N_{pe} spectra to calculate the gain correction factor. The corresponding $G^i_\alpha(R_{PMT})$ is shown in Figure 11. In this figure, the strong energy dependence of the multiple hit effect has disappeared at small R_{PMT}. The slight discrepancy at large R_{PMT} for the 3 MeV candle calibration is an artifact of the 10-hit hardware trigger, and poor energy resolution at low energy and large R_{PMT}.

One can then correct for the "gain" in both running scenarios on an event by event basis. For an event with a particular value of R_{PMT}, the gain-corrected signal N^{io}_α is

$$N^{io}_\alpha \;=\; G^i_\alpha(R_{PMT})N_i \qquad i = \mathrm{D_2O, NCD}; \alpha = N_{pe}, N_{hits}. \tag{4}$$

The means of N_{hits} and N_{pe} of gain corrected electron data sets are then used to form the energy calibration $C^i_\alpha(E)$ for each of the candle set. The resolution functions $R^\alpha_i(E)$ are also generated.

One can see how the multiple hit effect affects the energy calibration in this gain correction algorithm in Figures 12 and 13 in which $C^i_\alpha(E)$ and $R^i_\alpha(E)$ are displayed. In Figure 12, it is obvious that the slope of the energy calibration curve for the different candle sets is different using $G^i_\alpha(R_{PMT})$ extracted from N_{hits} information. For instance, the difference in the calibrated energy for 100 photomultiplier tube hits using the 3 MeV and the 15 MeV candle is 3% and 4% respectively in the pure D_2O and NCD installed running scenarios. On the other hand, the calibrated energy from using the N_{pe} information is well within the statistical fluctuation.
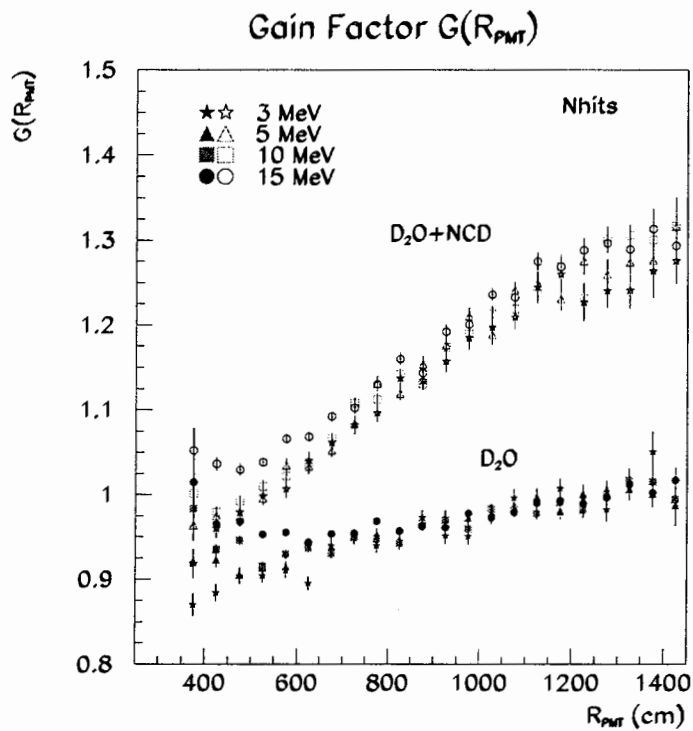
17

Figure 10: Energy dependence of $G(R_{PMT})$ for 3 MeV, 5 MeV, 10 MeV and 15 MeV candles. These plots demonstrate that $G(R_{PMT})$ is energy dependent when using only N_{hits} information. The discrepancies between the various "candle" calibration sets arise from the multiple hit effect especially at small R_{PMT}.
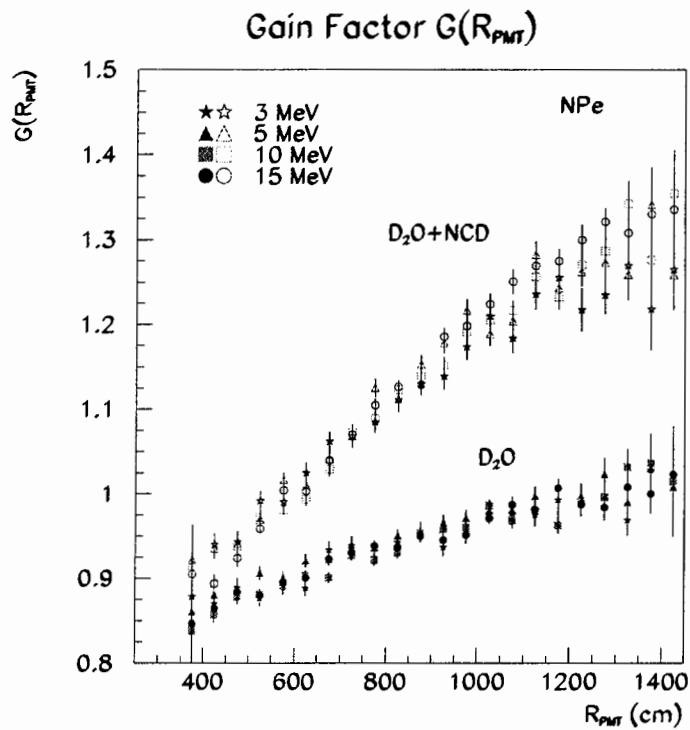
Figure 11: Energy dependence of $G(R_{PMT})$ for 3 MeV, 5 MeV, 10 MeV and 15 MeV candles . These plots demonstrate that the agreement in $G(R_{PMT})$ for small R_{PMT} is much better than the corresponding ones in Figure 10. The discrepancy at large R_{PMT} for the 3 MeV "candle" calibration is an artifact of the 10-hit hardware trigger, and poor energy resolution at low energy and large R_{PMT}.

This discrepancy indicates a shortcoming of the R_{PMT} gain correction scheme. Because of its simplicity, it does not take the detector asymmetry (e.g. neck of the acrylic vessel, NCD array) and other non-linear effects (e.g. multiple hits if dealing with N_{hits} spectrum) into account in a correct manner. From the goodness of agreement amongst different candle sets in the calibration curve extracted from N_{pe} information, it is clear that the detector asymmetry does not have much effect on this R_{PMT} gain correction technique. It is the non-linearity in the N_{hits} distribution which caused the break down of this technique. However, one can always use a multi-dimensional gain correction function to deal with this non-linearity correctly. Alternatively, one can use the N_{pe} information which is linear.

It is also clear from this analysis that the SNO detector response has a strong dependence on *both* the vertex position and the direction of the Čerenkov cone. Therefore, one must include these two dependencies into the detector gain correction scheme.

We want to emphasise once again the inadequacy of the "zeroth order approximation" outlined in Section 3.1. In the zeroth order analysis, the detector full-width-at-half-max N_{hits} resolution is $\sim$30% and $\sim$39% for 10 MeV electrons in the pure D_2O and the NCD installed scenarios. With the N_{hits} gain correction scheme, albeit there is a non-linear systematic effect arising from the multiple hit effect, the N_{hits} resolution for the NCD installed scenario has improved to $\sim$34% whilst the corresponding one in the pure D_2O run scenario remains at $\sim$30%.

3.3 Energy Response to γ Rays — Position and Directional Dependence

In the pure D_2O and the added salt running scenarios, the neutral current events are identified by the detection of the γ rays emitted subsequent to the neutron capture on deuterium or on chlorine nuclei. Photodisintegration background is also identified by the same channels. Therefore it is important to have a good understanding of the γ-ray response of the SNO detector.

To understand the γ-ray response, we use isotropic γ-ray events generated evenly throughout the D_2O volume. In Figure 14, the N_{pe}-R_{PMT} scatter plots are shown for 10 MeV γ rays in the pure D_2O and the NCD installed running scenarios. In these scatter plots, there is a long tail at small R_{PMT} which does not exist in the electron cases in Figure 7. If these raw γ-ray spectra are used to extract the R_{PMT} gain correction function as in Section 3.2, one would find that the correction function would drop off much more rapidly than the electron cases as R_{PMT} gets smaller. This indicates that the mean number of photoelectrons at small R_{PMT} in the γ-ray cases is much larger than that in the electron cases. This is also the origin of the slightly worse fit in the γ-ray N_{hits} and N_{pe} spectra in the "zeroth order approximation" as mentioned in page 7.

To understand the origin of this tail in the scatter plots, we replaced the acrylic vessel with D_2O in a test Monte Carlo run. In this latter run, the tail disappeared indicating that it is linked to the acrylic vessel. The explanation for this phenomenon is that Čerenkov light output is enhanced in the acrylic. The mean yield N of Čerenkov photons created in a track of length δx is [4]

$$N = \delta x \frac{\alpha}{c} \int_{\omega_1}^{\omega_2} \left(1 - \frac{1}{\beta^2 n^2}\right) d\omega \qquad (5)$$

where ω_1 and ω_2 are the frequency cutoffs, n is the refractive index and β is the relativistic factor. If one calculates the difference between the Čerenkov light yield in D_2O and in acrylic, one would
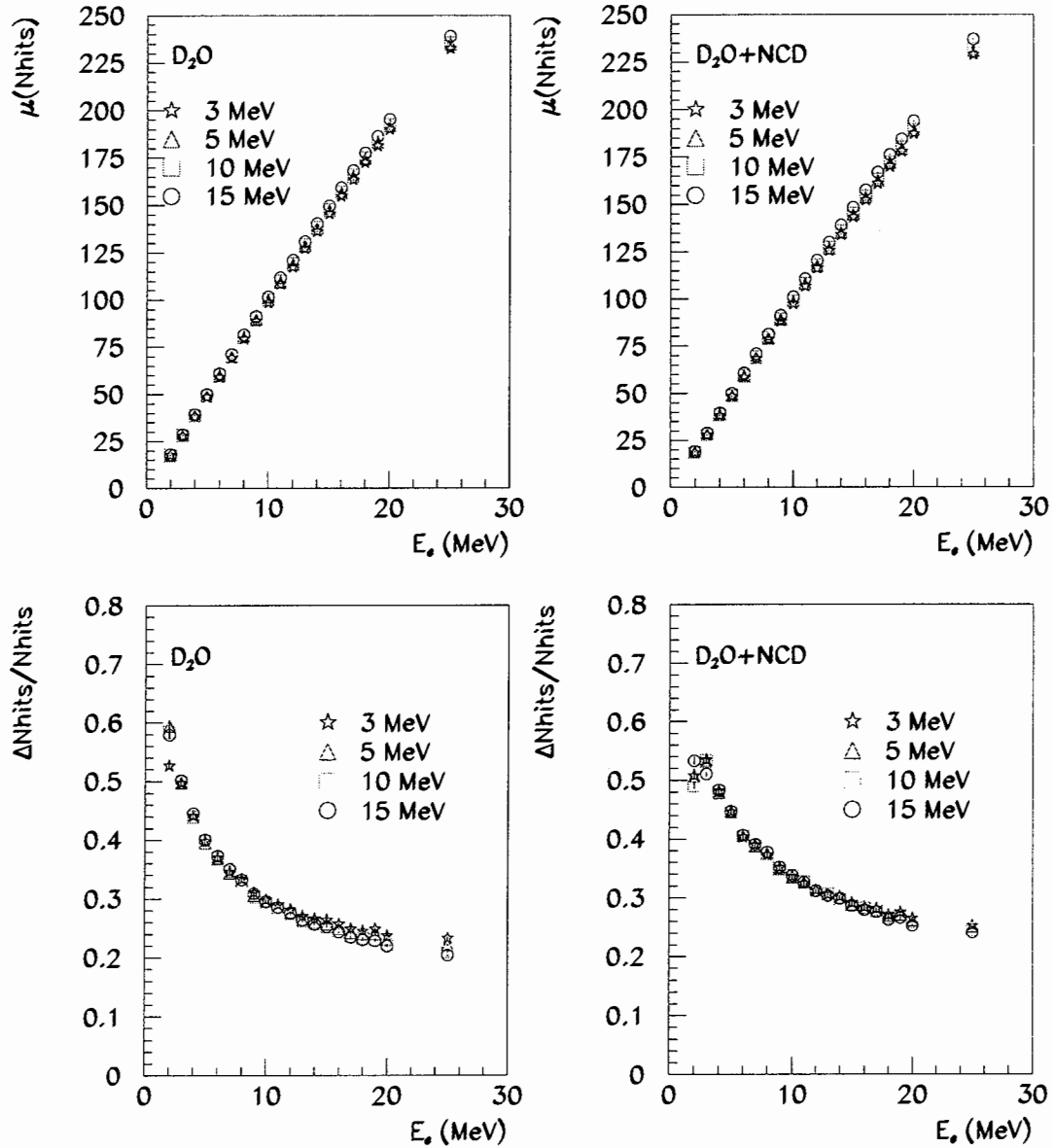
Figure 12: Calibration curves and energy resolution curves for different candle sets. The candle sets are 3 MeV, 5 MeV, 10 MeV and 15 MeV monoenergetic electrons. The gain correction functions extracted from N_{hits} distributions are used in these plots. It is clear that there is a non-negligible discrepancy between different candle sets.

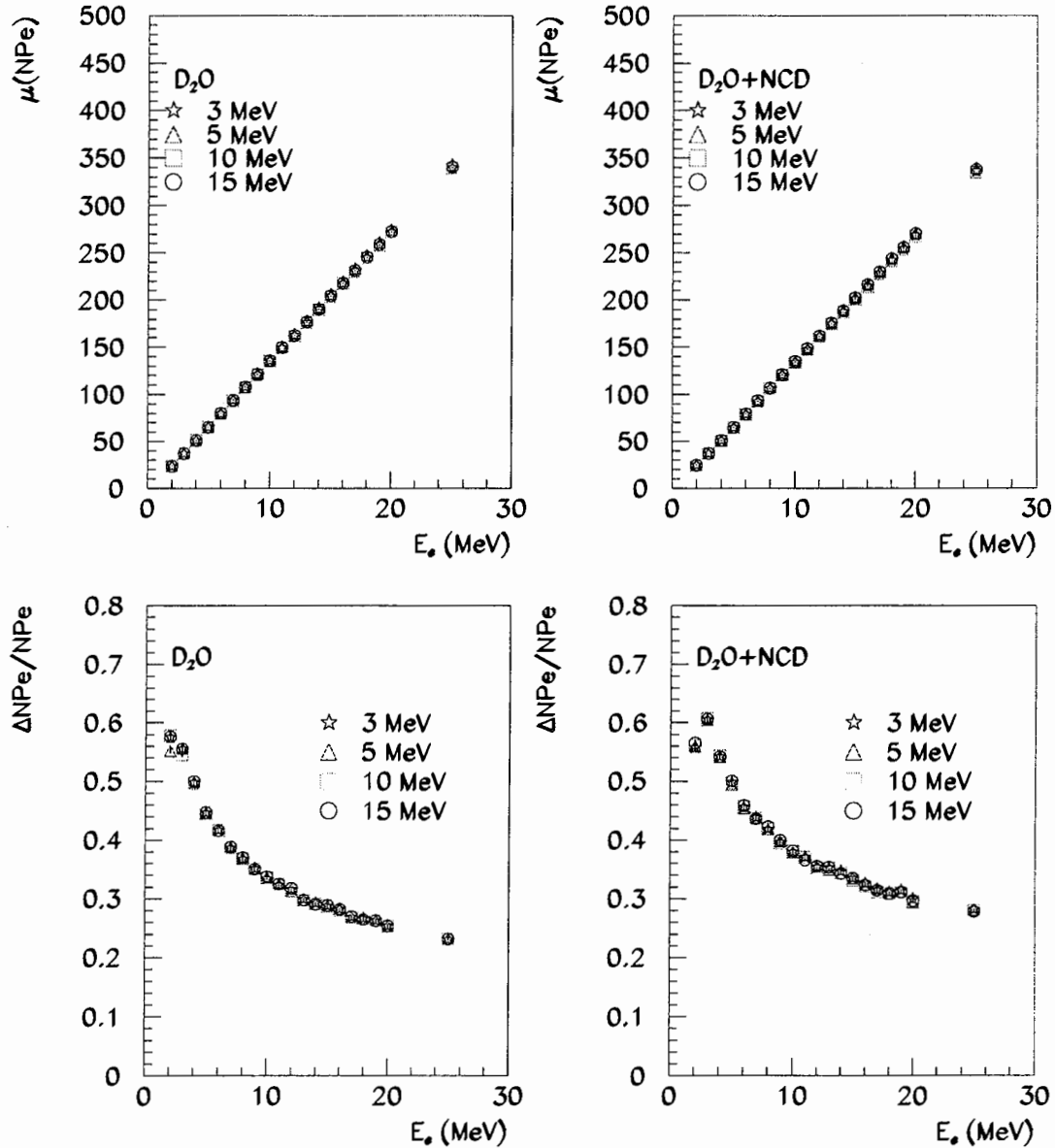## Monoenergetic Electrons (NPe Gain Corrected)

Figure 13: Calibration curves and energy resolution curves for different candle sets. The candle sets are 3 MeV, 5 MeV, 10 MeV and 15 MeV monoenergetic electrons. The gain correction functions extracted from N_{pe} distributions are used in these plots. The agreement between different candle sets is much better than the corresponding cases in Figure 12
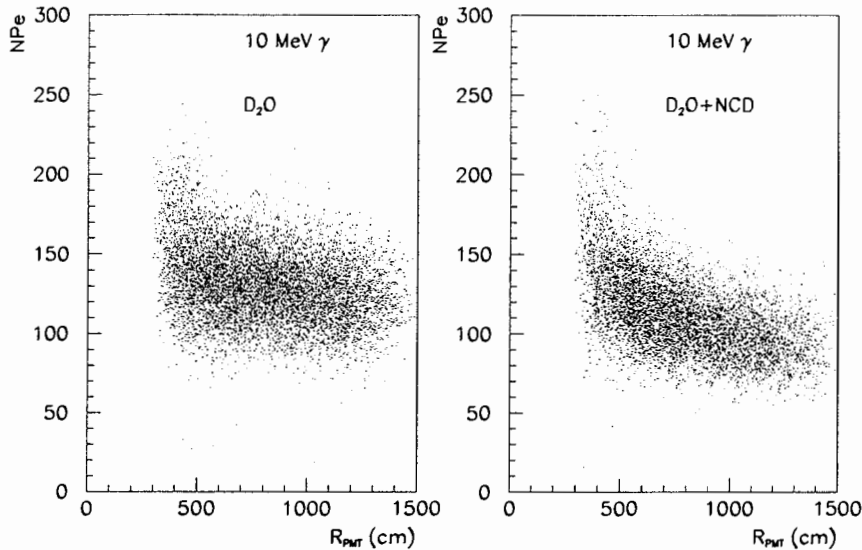
Figure 14: Dependence of N_{pe} on R_{PMT} for 10 MeV gamma rays in pure D_2O and NCD installed running scenarios.

find that there is a $\sim$20% difference.

An event generated close to and directed towards the vessel has a higher probability of converting into electron in the acrylic. These events are the ones with small R_{PMT}. To confirm this hypothesis, we put a spatial cut of $R \leq 500$ cm on the original γ-ray runs. This cut would only keep γ rays generated at least two attenuation lengths from the acrylic vessel, thereby reducing the number of γ rays converted in the acrylic. In Figure 15, it is clear that the tail in the N_{pe}-R_{PMT} appears in the $R > 500$ cm region. It is also obvious that these events close to the acrylic vessel generate many more multiple hits as there is a longer tail at the high end in the N_{pe}/N_{hits} histogram in the figure.

What this analysis on the SNO detector's response to γ rays has shown is that one must be very careful in handling γ-ray events originating close to the acrylic vessel. To correctly extract the neutral current energy spectrum in the added salt option or to extract the photodisintegration background signal, a careful γ-ray calibration near the acrylic vessel has to be done in order to determine the light output enhancement by the vessel.

4 Event Vertex and Direction Fitting Performance

As shown in Figure 4, an average of 15% of the light is lost when the NCD array is installed. We have demonstrated in the past section that this loss has a strong positional and directional
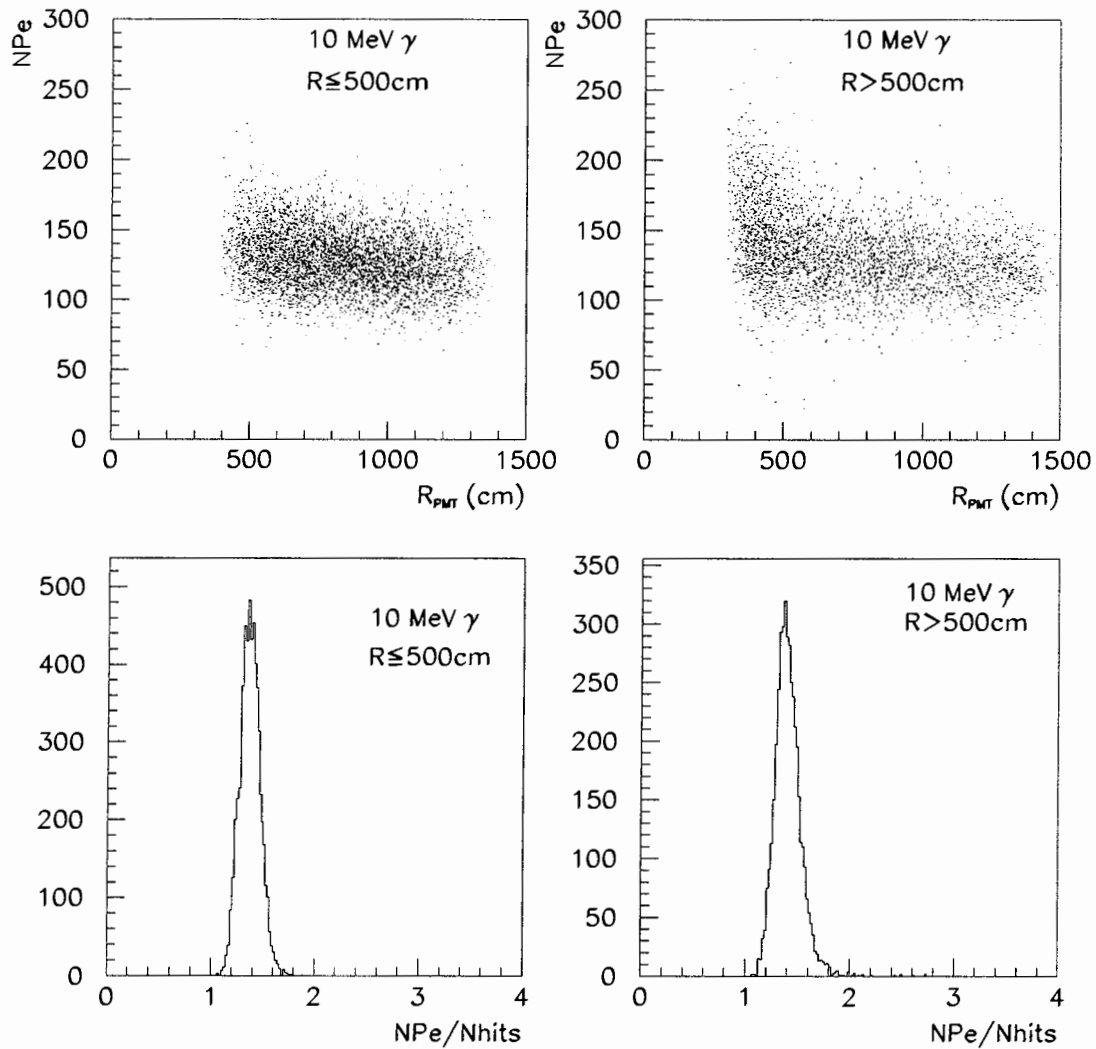
Figure 15: SNO detector response to 10 MeV gamma rays in the pure D_2O running scenario. *Top Left:* Scatter plot showing N_{pe} dependence on R_{PMT} with a spatial cut of $R \leq 500$ cm. *Top Right:* Scatter plot showing N_{pe} dependence on R_{PMT} with a spatial cut of $R > 500$ cm. *Bottom Left:* Number of photoelectrons per photomultiplier hit (N_{pe}/N_{hits}) for $R \leq 500$ cm. *Bottom Right:* Number of photoelectrons per photomultiplier hit (N_{pe}/N_{hits}) for $R > 500$ cm.

dependence as depicted in Figure 8. One concern is whether or not the event vertex and the electron direction can still be reconstructed reliably when the NCD array is in place. To answer this question, we compare the performance of the time fitter in SNOMAN 2.09 in the pure D_2O and the NCD installed scenarios. In this section, we shall first briefly introduce the time fitter, and we shall summarise our comparison of the time fitter performance under the two afore-mentioned running scenarios. We shall divide this investigation into two sub-categories: the vertex fitting performance in Section 4.2, and the directional fitting in Section 4.3.

4.1 The Time Fitter

In some sense, the time fitter has the simplest possible fitting algorithm. The fitter takes the positions $\vec{r_i}$ and the recorded time t_i of each of the hit photomultiplier tubes within the trigger, and calculates its event transit time deviation Δt_i defined as

$$\Delta t_i = \frac{1}{\langle c \rangle} |\vec{r_i} - \vec{r}| - (t_i - t),$$

(6)

where $\langle c \rangle$ is the average speed of light in the D_2O. If this transit time deviation is normally distributed, the best fit $(\vec{r}, t)$ is found when the χ^2 statistic

$$\chi^2 = \frac{1}{n-4} \sum_{i=1}^{n} \left[\frac{(\Delta t_i)^2}{\sigma_i^2} \right]$$

(7)

is minimised. In the default SNOMAN 2.09 settings, photomultiplier tube hits that occur 8 ns earlier or 4 ns later than the fitted t are not used in the fit in order to reduce the effects of photomultiplier noise and scattered light.

4.2 Vertex Fitting Performance

Good vertex fitting resolution is critical to discriminating background events in the SNO detector. The time fitter, because of its simplicity, gives us a lower bound estimate on this resolution. To determine the effects the NCD array has on the time fitter's vertex fitting ability, we compare its performance on monoenergetic electrons and γ rays generated isotropically and evenly in the D_2O volume under the two running scenarios. As an example, scatter plots displaying the dependence of the time fitter reconstructed radial distance R_{fit} on the Monte Carlo generated radial distance R for 10 MeV electrons in the two running scenarios are shown in Figure 16.

For each electron energy data set, we fit each of the R_{fit}-R scatter plots to a linear relationship. We then compare the difference in linearity between the two running scenarios by taking the ratio of their respective slopes. These results are summarised in Figure 17. These plots indicate that the introduction of the NCD array does not affect the linearity of the time fitter's vertex fitting ability.

With the fact that the presence of the NCD array does not introduce any non-linear artifact in the vertex fitting established, the question of the accuracy of the vertex fit was investigated. To determine this accuracy, we look at the distribution of R_{dev}, which is the distance between the fitted vertex and the Monte Carlo generated vertex:

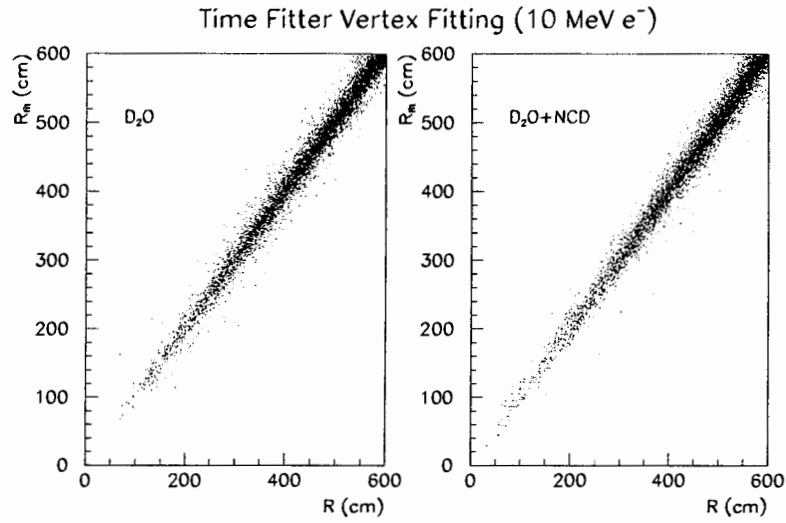$$R_{dev} = |\vec{R}_{MC} - \vec{R}_{fitted}|,$$

(8)

Figure 16: Scatter plots showing time fitter reconstructed radial distance in the two running scenarios for 10 MeV electrons.
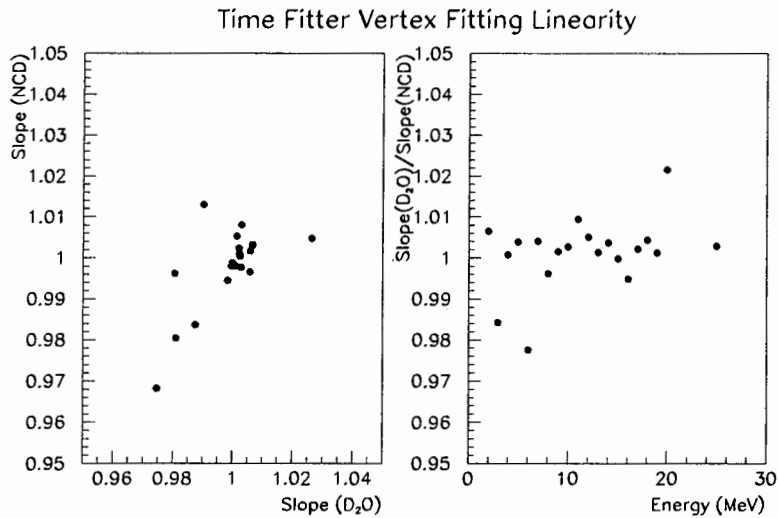

Figure 17: Linearity of the time fitter. *Left:* scatter plot showing the fitted slope for the $R_{fit}R$ relation at different electron energies; *Right:* plot showing the ratio between the fitted slopes in the D_2O and the NCD installed scenario.
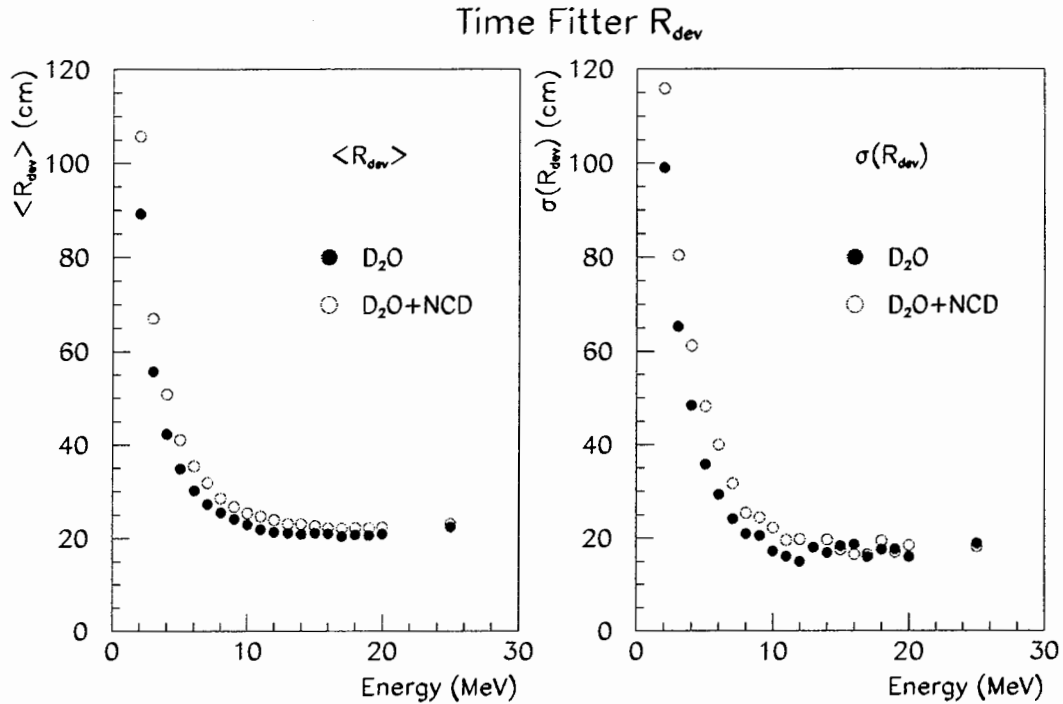
Figure 18: Deviation of the time fitter fitted radial distance for electrons. *Left:* The average radial distance deviation; *Right:* The standard deviation of the radial distance deviation.

where $\vec{R}_{MC}$ and $\vec{R}_{fitted}$ are the Monte Carlo generated and the time fitter fitted vertices. In Figures 18 and 19, the mean and the standard deviation of the R_{dev} distribution for electrons and γ rays are shown. From Figure 18, the deviation levels off as energy increases for electrons whilst the deviation appears to increase at higher energies in the γ-ray case. The drop of the mean R_{dev} as energy increases at low energy is attributed to the increased Čerenkov photon statistics for both electrons and γ rays. However, as the γ ray energy increases, its attenuation length also increases. As a result, the mean R_{dev} increases at high γ-ray energies, whilst that of the electrons reaches a plateau. At an energy of 2 MeV, the average R_{dev} gets worse by less than 20 cm for both electrons and γ rays in the NCD installed scenario when compared to the pure D_2O scenario. This is essentially a statistical effect because of light absorption by the NCD array.

4.3   Directional Fitting Performance

An accurate fitting of the Čerenkov cone direction is essential in separating the different classes of events in the SNO detector. For instance, it is desirable to be able to separate the charged current and the elastic scattering events in the NCD installed scenario. Therefore, we have investigated the directional fitting performance of the time fitter in the two running scenarios.
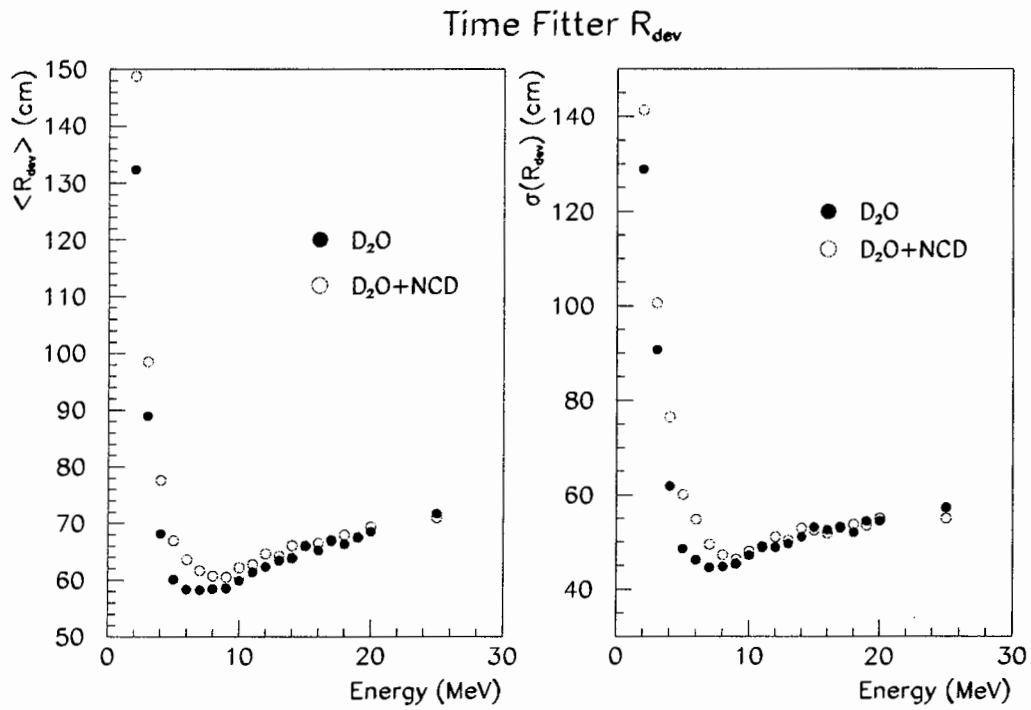
27

Time Fitter R$_{dev}$

Figure 19: Deviation of the time fitter fitted radial distance for γ rays. *Left:* The average radial distance deviation; *Right:* The standard deviation of the radial distance deviation. The rise at high energies is attributed to the increased γ-ray attenuation length.

Similar to the vertex fitting analysis in the last section, we first try to determine if there is any non-linear effect in the direction fitting in the electron cases when the NCD array is in place. We came to the same conclusion as in the vertex fitting case that the NCD array does not introduce any non-linearity.

To determine the accuracy of the directional fitting, we look at the angular deviation ψ defined as

$$\cos(\psi) = \frac{\vec{R}_{MC} \cdot \vec{R}_{fitted}}{|\vec{R}_{MC}||\vec{R}_{fitted}|}. \tag{9}$$

That is, ψ is the opening angle between the Monte Carlo generated direction and the time fitter fitted direction. In Figure 20, the normalised $\cos(\psi)$ distribution for 10 MeV electrons generated evenly and isotropically in the D_2O volume is shown. From this figure, it is clear that the fitted directional resolution is slightly worse in the NCD installed case.

To understand this degradation quantitatively, we can look at Figures 21 and 22. In these figures, the mean and the standard deviation of the ψ distributions for monoenergetic electrons and γ rays are plotted against energy. These plots demonstrate that the effects of photon absorption and scattering off the surface of the NCD counter body on the direction fitting performance are small as the difference between $< \psi >$ in the pure D_2O case, and that in the NCD installed case are less than 2° for both the electrons and the γ rays in the energy range we investigated.

In conclusion, we do not see any significant degradation in the time fitter's ability to reconstruct events in the NCD array running scenario. The slight degradation in time fitter performance with the NCD array in place is mainly a direct consequence of the reduction of photon statistics for the fitting. The NCD array does not introduce any non-linear effect which would severely compromise the fitter performance.

5   Energy Spectrum of Charged Current Signal

One of the goals of the SNO detector is to look for a possible shape distortion in the energy spectrum of the charged-current (CC) signal. Because the presence of the NCD array would inevitably deteriorate the energy resolution of the photomultiplier tube array, it is necessary to understand how this effect would affect SNO detector's ability to detect a spectral distortion in the charged-current signal. We shall devote our discussion in this section to the SNO detector's ability to detect this shape distortion in the presence of the NCD array.

Three sets of 1-year CC data at full standard solar model (SSM) rate for both pure D_2O and NCD installed scenarios were generated. All the generated events are gain corrected in N_{pe} and energy calibrated as described in Section 3.2. A theoretical spectrum was also generated using the CC energy generator in SNOMAN. This latter spectrum was then convoluted with the gain corrected energy resolution in Figure 13. We chose to compare these spectra without introducing further complication such as fitter effects. Hence, we used the raw Monte Carlo event output instead of the fitter fitted vertex and direction for the gain correction. This is justifiable given the time fitter performance analysis in Section 4. We then compare the energy convoluted CC spectrum with the corresponding gain corrected Monte Carlo results by the Kolmogorov-Smirnov (K-S) test. In
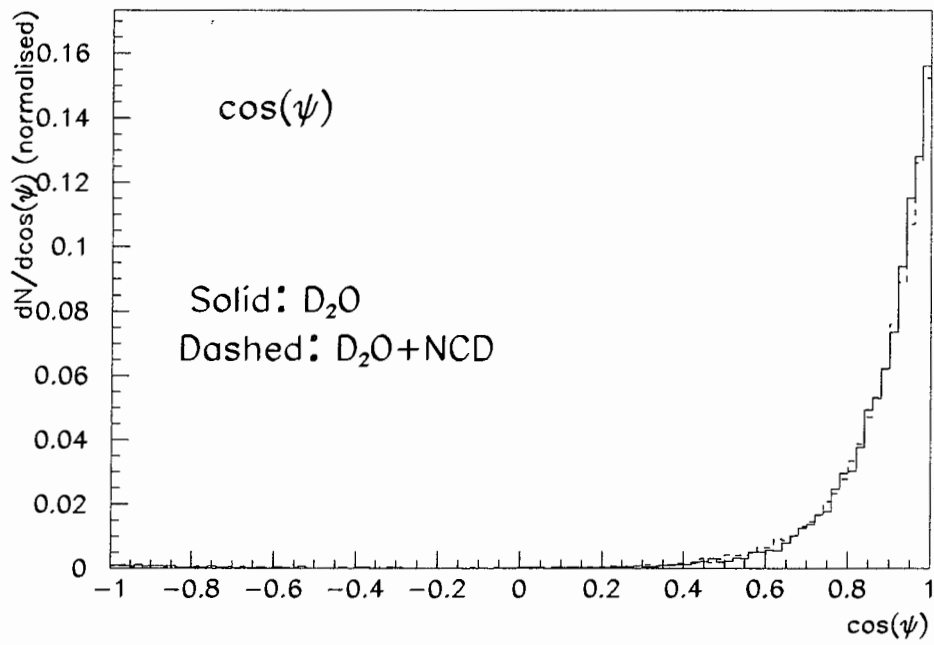
29

Figure 20: Normalised distribution of $\cos(\psi)$ for 10 MeV electrons. The solid line is the pure D_2O running scenario, whilst the dashed line is the NCD installed scenario.
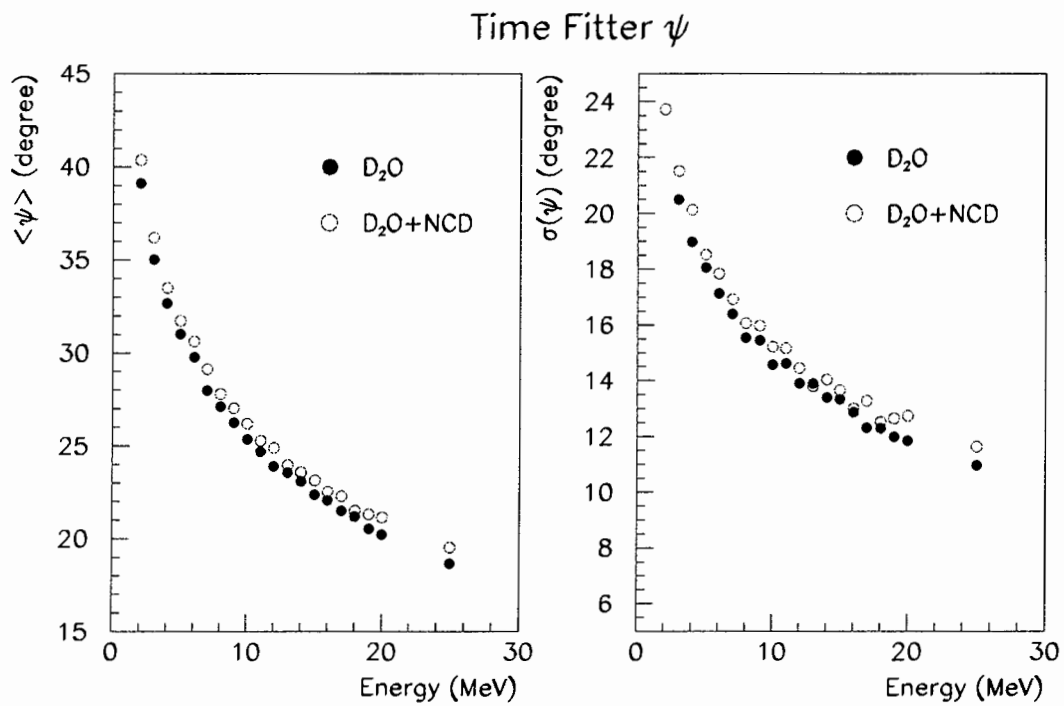
Time Fitter ψ

Figure 21: Opening angle ψ between the fitted direction and the Monte Carlo generated direction for electrons. *Left:* The mean of ψ distribution; *Right:* The standard deviation of the ψ distribution.
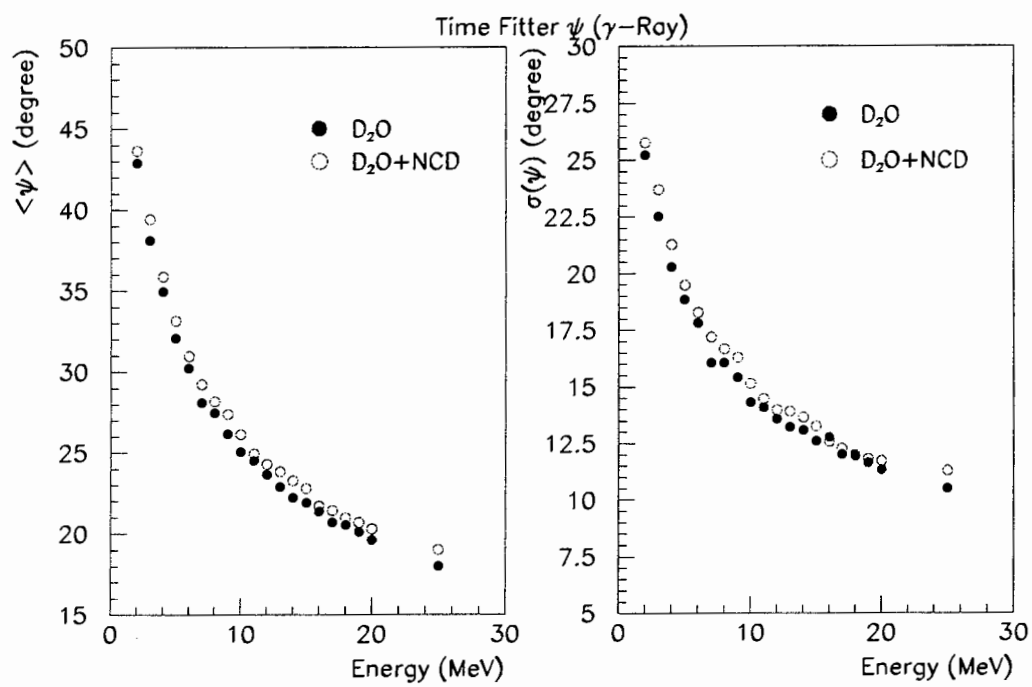
Figure 22: Opening angle ψ between the fitted direction and the Monte Carlo generated direction for γ rays. *Left:* The mean of ψ distribution; *Right:* The standard deviation of the ψ distribution.

Run	$\Pr_{D_2O}$	$\Pr_{NCD}$
1	0.723	0.999
2	0.942	0.835
3	0.989	0.942

Table 4: Kolmogorov-Smirnov probability for comparing the theoretical CC spectrum convoluted with the gain corrected resolution function and the N_{pe} gain corrected, energy calibrated Monte Carlo spectrum. The Monte Carlo event sets consist of one-year of CC events at full standard solar model rate. These results indicate that the gain correction scheme can reproduce the CC spectrum in a self-consistent manner.

Section 6, we shall do a "realistic" analysis with all the signals being analysed first by the time fitter.

In Table 4, we list the K-S probabilities for the null hypothesis of the spectra being drawn from the same distributions for the three data sets in each of the run scenarios. It is clear from the table that the gain correction scheme does reproduce the CC spectrum in a self-consistent manner, whether or not the NCD array is in place. In Figure 23, we show how the three year full SSM CC spectra compare.

In order to understand the sensitivity of this spectrum comparison to the energy calibration, we make an overall shift in the energy calibration function $C(E)$ and the energy resolution function $R(E)$ in Figure 13. In particular, we shift these functions in one of two ways:

1. $C(E) \rightarrow C(f_C E)$

2. $R(E) \rightarrow R(f_R E)$,

where f_C and f_R are the overall gain shift factors. In other words, if f_C does not equal to unity, the overall gain on the calibrated Monte Carlo CC spectrum will be offset by a factor of f_C. On the other hand, if f_R does not equal to unity, the energy resolution function used to convolute the theoretical CC spectrum is offset by a factor of f_R in the energy scale. In Table 5 we summarise our findings of this systematic analysis. In this analysis, we use 3-year-equivalent CC spectra.

From Table 5, it is clear that an introduction of an overall gain shift of as small as 1% would cause a non-negligible change to the shape of the observed CC energy spectrum. A similar statement can also be made for the energy resolution function. However, what this analysis has demonstrated is that the R_{PMT} gain correction technique is a self consistent technique which can reconstruct energy spectra to much better than 1%. This analysis has also shown that the CC energy can be reconstructed, without any significant distortion, when the NCD array is in place.
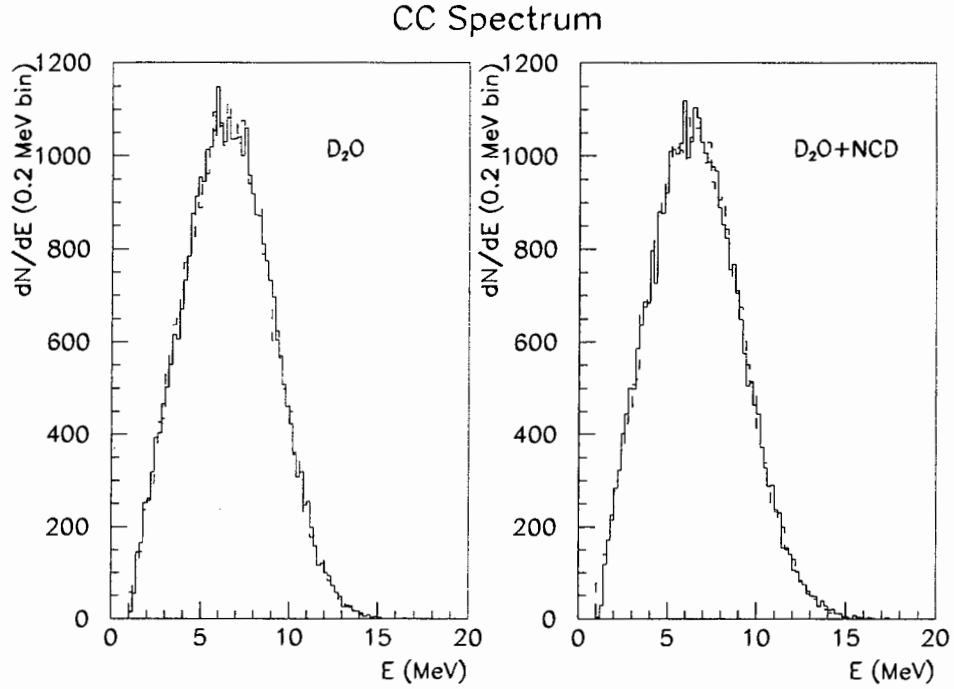
CC Spectrum

Figure 23: Three year data set of CC spectra. The dashed histograms in these two graphs are the energy resolution convoluted theoretical spectra. The gain corrected Monte Carlo spectra are shown as solid histograms.

$f_C(E)$	$f_R(E)$	Pr_{D_2O}	Pr_{NCD}
0.98	1.00	$< 10^{-5}$	$< 10^{-5}$
0.99	1.00	0.002	0.016
1.00	0.98	$< 10^{-5}$	$< 10^{-5}$
1.00	0.99	0.002	0.024
1.00	1.01	0.117	0.007
1.00	1.02	$< 10^{-5}$	$< 10^{-5}$
1.00	1.00	5×10^{-5}	0.004
1.02	1.00	$< 10^{-5}$	$< 10^{-5}$

Table 5: A test of the sensitivity of the CC energy spectrum to the energy calibration and the energy resolution functions.

6   Gain Correction Factor Calibration in the SNO Detector

So far we have considered using only the "hypothetical" calibration sources—monoenergetic electron sources—to calibrate R_{PMT}. In reality, the only way to generate high energy monoenergetic electrons is to use an electron accelerator. This scheme will also involve designing complicated beam optics to bring the electrons to various parts of the SNO detector for the gain calibration. This is a very difficult task indeed.

However, in the arsenal of the SNO calibration sources, two of the γ-ray sources might be suitable for this R_{PMT} calibration. These are the ^{16}N and the ^{3}H$(p,\gamma)^{4}$He sources. The ^{16}N emits a monoenergetic 6.13 MeV γ ray, whilst the ^{3}H$(p,\gamma)^{4}$He source generates a 19.8 MeV γ ray.

Throughout this report, we have been using the Monte Carlo generated vertex and direction for the gain correction algorithm. In reality, we do not have the luxury of knowing the origin of the events in the SNO detector. Therefore, we have to apply all the techniques we have been developing in the previous sections in a more realistic setting.

In this section, we shall first generate the gain correction function using γ-ray events and time fitter fitted parameters. We shall then compare this function with that generated with electron events. Subsequently, we shall perform a charged current energy spectrum analysis as in Section 5 using this gain correction function.

6.1   Extracting the Gain Correction Function Using γ Ray Events

We shall first look at a similar plot to Figure 14 for the parameter R_{PMT}^{fit} defined as

$$R_{PMT}^{fit} = -R\cos\delta^{fit} + \sqrt{(R_{fit}\cos\delta^{fit})^2 + \rho^2 - R_{fit}^2} \tag{10}$$

where R_{fit} is the radial distance of the time fitter fitted vertex, δ^{fit} is the opening angle between the fitted position vector of the vertex and the fitted direction of the outgoing track. In essence, this relation is the same as Eqn.(2) with time fitter fitted parameters replacing the Monte Carlo generated parameters. An N_{pe}-R_{PMT}^{fit} scatter plot for 10 MeV γ rays generated evenly and isotropically in the D$_2$O volume is shown in Figure 24. In this plot, a spatial cut of $R_{fit}{\leq}600$ cm is placed.

A striking difference between Figures 24 and 14 is that the tail which exists in the small R_{PMT} region in the latter figure no longer appears in the former one. This can be explained by the fact that the time fitter tends to reconstruct the event vertex closer to the photomultiplier tube array than the actual vertex. Therefore, outward-going events generated near the acrylic vessel are more likely to get reconstructed outside the active D$_2$O volume. Combining this fact and the γ-ray attenuation length, one can see that most of the γ-ray events that would have been converted into electrons in the acrylic vessel are reconstructed outside the active D$_2$O volume by the time fitter. With this spatial cut at $R_{fit}{\leq}600$ cm, Figure 24 resembles the corresponding plot for electron events. Therefore, it is possible to apply the gain correction technique we have been using on electron events to these γ-ray events.

The gain correction functions extracted from these time fitter fitted γ rays can be compared to the ones extracted from the time fitter fitted electrons. We find that the gain functions extracted from
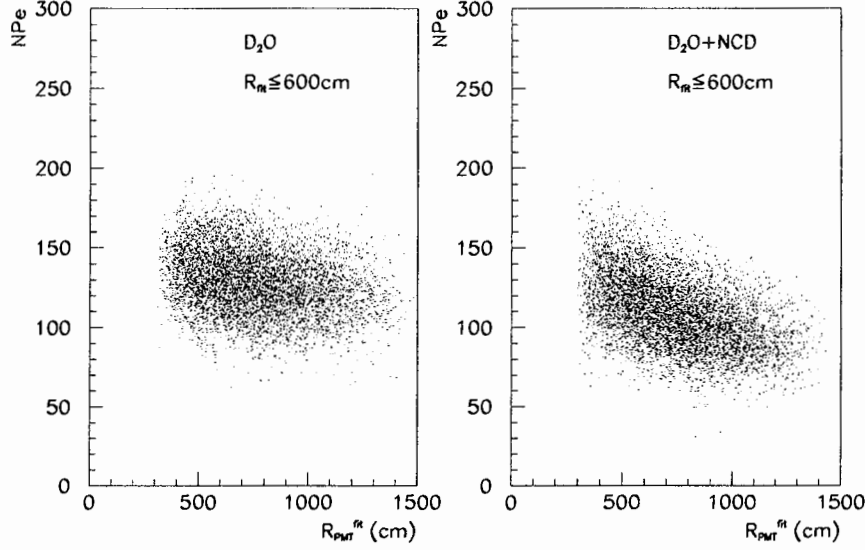
Figure 24: Dependence of N_{pe} on R_{PMT}^{fit} for 10 MeV gamma rays in pure D_2O and NCD installed running scenarios. A spatial cut of $R_{fit} \leq 600$ cm is placed on the data.

the γ rays are consistently higher than the electron ones in both running scenarios. This difference arises from the fact that γ rays have to travel a certain distance before converting to an electron. It is this electron vertex which the time fitter fits. Therefore, there is an offset between the gain correction functions extracted from γ rays and from electrons. We shall now demonstrate how we can shift the γ-ray extracted gain correction function to correspond to the electron extracted function.

In Section 3.2, the extracted gain curves are fitted to fourth-order polynomials. By the definition of the gain correction function in Eqn.(3), it is an approximation of the amount of optical light attenuated in the SNO detector. Hence, we would expect

$$G_\alpha^i(R_{PMT}^{fit}) \; \propto \; \exp\left(\lambda R_{PMT}^{fit}\right) \qquad i = D_2O, \, NCD; \alpha = N_{pe}, N_{hits} \tag{11}$$

where λ is an average attenuation length for optical photons propagating through the D_2O, acrylic vessel and the light water. We can therefore expect λ to be of the order of the optical light attenuation length in the D_2O. Because $\lambda R_{PMT}^{fit} \ll 1$, we can fit the gain function to a linear form:

$$G_\alpha^i(R_{PMT}^{fit}) \; = \; \sum_{i=0}^{1} a_i R_{PMT}^{fit,i}. \tag{12}$$

To correct for the shift of the gain correction function extracted from γ rays, we shift the linear fit of the gain correction function from electrons in R_{PMT}^{fit} to correspond to the γ-ray one. In Figure 25, the linear fit to the electron gain correction function in the pure D_2O running scenario is shifted to
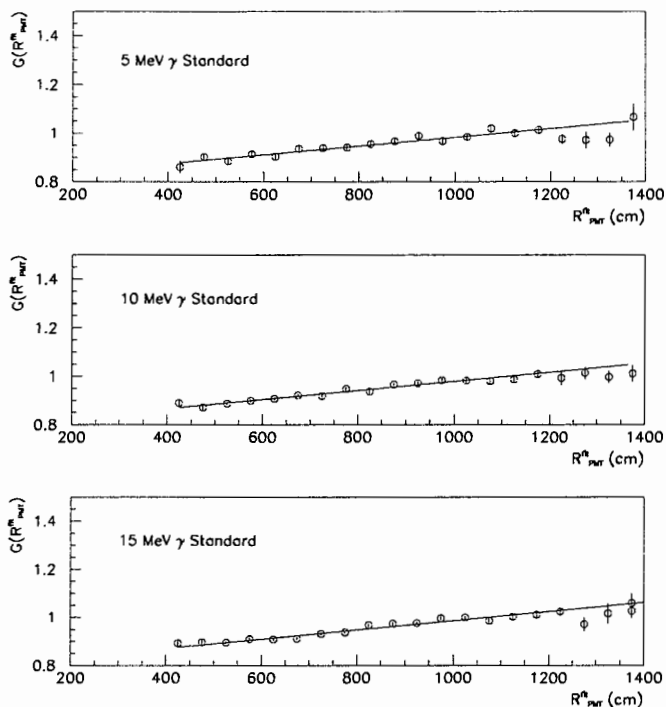
36

Figure 25: Matching the gain correction functions generated from electron events and from γ-ray events in the pure D_2O running scenario. The average R^{fit}_{PMT} shift for these three γ candles is (57 ± 7) cm.

match the correction function extracted from γ-ray events for the different γ-ray candles. We find that there is an average R^{fit}_{PMT} shift of (57 ± 7) cm amongst the three γ candle sets we use. A similar analysis on the NCD installed scenario demonstrate that an average R^{fit}_{PMT} shift of (29 ± 3) cm is needed to match the gain correction functions generated from the two different classes of events.

6.2 Energy Calibration and Spectral Reconstruction

In the last section, we have demonstrated the algorithm to extract the gain correction functions from γ-ray events. In this section, we shall apply these functions to construct energy spectra.

To demonstrate that the algorithm in the last section does reproduce the energy calibration curve and the detector resolution curve extracted from electron gain correction function, we use the gain correction functions extracted from electron events and γ-ray events to gain correct monoenergetic isotropic electrons generated evenly throughout the D_2O volume. Plots similar to Figure 13 are produced. When comparing the energy calibration curves extracted from using the two different classes of gain correction function, the difference between them is less than 0.5 photoelectron at 10 MeV.
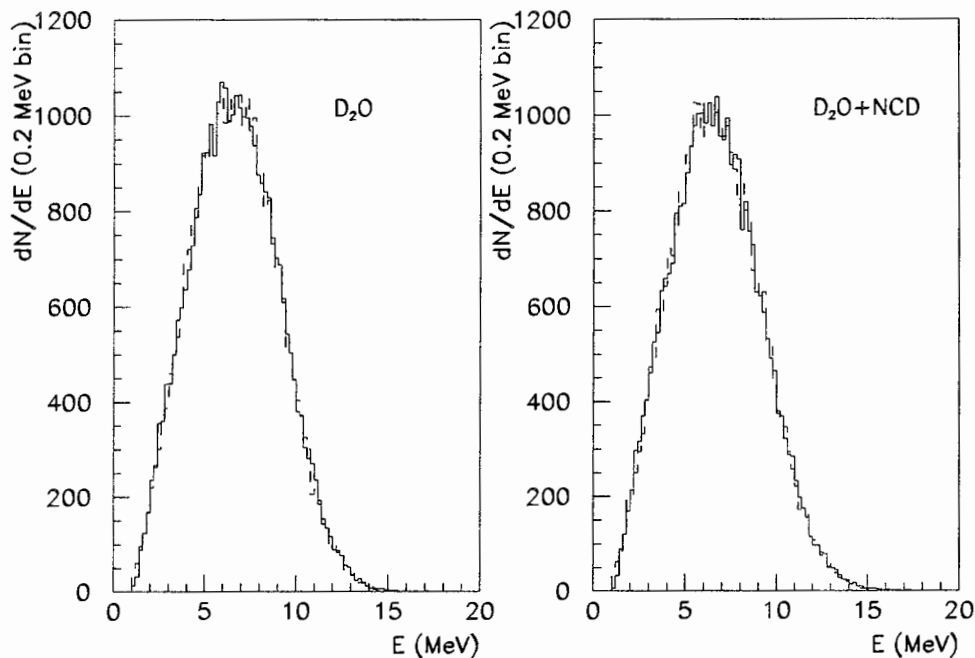
37

CC Spectrum (γ Gain Calibrated)

Figure 26: Reconstructed charged current spectra. These spectra demonstrate that it is possible to use γ rays to calibrate the gain correction function. The solid histograms are the gain corrected and energy calibrated Monte Carlo spectra. The dashed histograms are theoretical spectra convoluted with the detector resolution function.

Finally, we repeat this exercise for the charged current energy spectrum. We use energy spectra correspond to three years of charged current events reconstructed inside the D_2O volume. In Figure 26, the Monte Carlo N_{pe} spectrum is gain corrected and energy calibrated using the gain correction functions extracted from γ-ray events. This spectrum is then compared with the theoretical spectrum convoluted with the detector resolution. A K-S test shows that the probability for the null hypothesis is 0.83 and 0.70 for the pure D_2O and the NCD installed running scenarios.

In summary, we have demonstrated that it is possible to extract the gain correction functions from monoenergetic γ rays. One merely has to shift the functions in R_{PMT}^{fit} to correct for the distance the γ rays have to travel before converting to electrons. The question of optimising this calibration procedure by deploying γ-ray sources at discrete points inside the D_2O volume is under investigation. The results of this investigation warrants a separate report.

7 Conclusions

When the NCD array is in place, the position dependence of the SNO detector response is stronger. In addition, the array reduces the number of detected Čerenkov photons by about 15%. However, we have demonstrated in this report that when this position dependence is corrected by the R_{PMT} gain correction, the NCD array does not introduce any non-linear systematic artifact. In addition, there is no significant degradation of the time fitter performance. Given that the time fitter is the simplest fitter of all, we do not anticipate the presence of the NCD array would degrade the performance of other more sophisticated fitters.

We have identified a systematic feature of enhanced Čerenkov light output for γ rays converted in the acrylic vessel. A γ-ray calibration near the acrylic vessel is necessary to get the correct γ-ray response of the SNO detector.

We have demonstrated that the R_{PMT} "gain correction" technique is a practical algorithm to correct for the position dependent response of the SNO detector. Even though it does not take into account the asymmetry of the SNO detector incurred by the presence of the neck of the acrylic vessel, this simple algorithm is capable of reconstructing the energy spectrum reliably using the N_{pe} information. An astute reader would realise that any energy spectrum gain corrected by the N_{pe} information would have a wider width because the calibrated charge from the electronics is used (see Section 3.1). As mentioned in that Section, we are investigating different techniques to "quantise" this calibrated charge. We anticipate that a "quantised" analysis would only improve the energy spectrum discriminatory ability of this technique due to improved resolution.

We have investigated the problem of using γ rays to construct the R_{PMT} gain correction in a "realistic" analysis. In this analysis, the γ-ray events are reconstructed by the time fitter. The resulting gain correction function extracted from this reconstruction has to be corrected for the γ ray attenuation length before it is useful for gain correcting electron signals. Our results indicate that one can accurately reconstruct energy spectra with this technique.

References

[1] The SNOMAN authors, *The SNOMAN User's Manual, Version 2.09*, 1996

[2] C.E. Waltham, 1996. Private communication.

[3] M. Lay, *Energy Response and PMT Backgrounds in SNO*, SNO internal report STR-96-015.

[4] J.V. Jelley, *Čerenkov Radiation*, Pergamon Press, London (1958).